Computational Statistics
https://doi.org/10.1007/s00180-025-01645-y

ORIGINAL PAPER

# Monitoring time dependent image processes for detecting shifts in pixel intensities

**Yarema Okhrin**[1] · **Viktoriia Petruk**[2] · **Wolfgang Schmid**[2]

Received: 15 May 2024 / Accepted: 23 May 2025


**Abstract**
The problem of shift detection in image processes is addressed in this study. It is assumed that the pixel intensities follow a spatial autoregressive process, and potential shifts manifest in average intensities. The objective is to detect shifts as quickly as possible after their occurrence. To accommodate high-resolution images, a scalable technique is suggested, focusing on the surveillance of regions of interest. For shift detection, multivariate exponentially weighted moving average (EMWA) control schemes and various types of control statistics are employed. The efficiency of the proposed unique approach is demonstrated through an extensive simulation study. Additionally, recommendations for practitioners are provided regarding the selection of the chart, its setup, and calibration.

## 1 Introduction

The simplicity of taking and storing images leads to an increasing importance of image-type data not only in social media but also in manufacturing, economics, medicine, engineering, etc. Moreover, we often consider not only a single isolated image, but a sequence of images observed or taken with a given frequency at fixed time periods. The general aim is to extract meaningful and useful information from

✉ Yarema Okhrin
yarema.okhrin@uni-a.de

Viktoriia Petruk
petruk@europa-uni.de

Wolfgang Schmid
schmid@europa-uni.de

[1] Chair of Statistics and Data Science, Faculty of Business and Economics, University of Augsburg, Augsburg, Germany

[2] Department of Statistics, Faculty of Business and Economics, Europa-Universität Viadrina, Frankfurt (Oder), Germany

Published online: 03 July 2025

this sequence and use it for further problem-driven analysis. Furthermore, the resolution of images has dramatically increased in recent years and the number of possible applications of images became very heterogeneous. Therefore, statistical and econometric tools became of great importance for analyzing this kind of data.

An ordered sequence of images can be seen as a realization of a stochastic process. Each image is characterized by the set of pixels, their coordinates, color, and intensity. This results in a time series of multivariate spatial data and its modelling became an important field of research in statistics. The objective of the analysis typically deals with issues in feature extraction, image classification, image transformation, etc. Popular statistical methods, such as multivariate time series models, Kalman filtering, Markov random fields, hidden Markov processes, Bayesian approaches, etc. need to be adjusted to handle this type of data and to offer solutions for the above problems. An excellent overview can be found in, e.g., Fieguth (2010).

In this paper, we focus on monitoring changes in a sequence of images using methods of statistical process control. This application is of particular importance for production processes that use digital imaging for quality assurance. For example, a company wishes to detect the violation of the specified quality requirements as soon as possible. It uses for this purpose a suitable imaging equipment. These ideas can also be applied in other fields, for example, in medicine for early detection of tumors, vascular changes, etc. An excellent overview of control charts for images is given in Megahed et al. (2011). Horst and Negin (1992) were the first to apply control charts to image data, with a special focus on web applications. In Armingol et al. (2003) illumination changes through a transformation of the pixel values are controlled. The authors construct individual moving-range control charts for each pixel. Hotelling's $T^2$ control chart was widely applied in image analysis, e.g., by Mason et al. (1997), Tong et al. (2005) and Liu and MacGregor (2006). Lin (2007a) and Lin (2007b) use a combination of multivariate control charts and wavelets to detect defects in electronic components. Lin et al. (2008) compare a wavelet with an imposed Hotelling's $T^2$ control chart with a wavelet and a principal component approach to detect faults in LED chips. Jiang et al. (2005) used a spatially exponentially weighted moving average chart to find defects in LCD monitors and Lu and Tsai (2005) used a spatial $\bar{x}$ chart for the same application.

Koosha et al. (2017) suggest a non-parametric regression method to extract features from grayscale image data. The resulting features are monitored to detect out-of-control situations using a generalized likelihood ratio (GLR) control chart. Amirkhani and Amiri (2020) present a defect detection method for image processes, segmenting images into regions of interest (ROIs) and applying a $p$-value-based control chart based on analysis of variance (ANOVA). Dunnett's test is used to localize defects, and a simulation study compares performance metrics with a prior monitoring approach of Koosha et al. (2017). A case study on tile production provides practical guidelines, though it relies on simulated defects rather than real-world images. Yeganeh and Shadman (2021) does not handle image monitoring directly but proposes a novel artificial neural network to monitor logistic profiles, using average run lenghth (ARL) as a performance criterion. Results are compared with multivariate exponentially weighted moving average (MEWMA) and likelihood ratio test (LRT) approaches. Okhrin et al. (2020) consider and compare several monitoring schemes

applied to the characteristics of ROIS. Contrary to most of the previous literature, they take into account a spatial dependence between the pixel intensities. Dastoorian et al. (2022) review different shift types in previous control charting approaches, and focus then on academically unexplored but relevant shift types in high-density spatial data. The use of information from several images simultaneously was explored in Chen and Wells (2022). The authors apply multilinear principal component analysis (MPCA) to fuse several images into a single one and deploy single-image MEWMA for monitoring purposes. Frequently, one observes both an image and an additional numeric data. A regression-based approach is introduced in Eslami et al. (2023) to monitor image data as geometric profiles, using wavelet transformation to extract large-scale features and a generalized likelihood ratio (GLR) control chart for monitoring. Small-scale features are analyzed with an omnibus control chart, considering both spatial and temporal correlations. The method is validated on a real carpet production process and includes a useful flowchart. Dastoorian and Wells (2023) deal with this problem by suggesting a hybrid monitoring technique that uses MPCA too. Yeganeh et al. (2024) develop an ensemble control chart approach to enhance the performance and computational efficiency of control charts for image data. Yao et al. (2024) proposes a method for monitoring large images by splitting them into non-overlapping sub-images and using two-dimensional input multi-variate functional principal component analysis (2D-MFPCA) to capture spatial correlations. A global multivariate cumulative sum (MCUSUM) statistic is used for monitoring, with ARL as a performance measure. The case study involves a digital twin of a 3D scanning system to detect uneven surface defects on vertical structures. A CUSUM-type control chart for online grayscale image monitoring is proposed in Roy and Mukherjee (2025), aiming to detect small changes while preserving edges and textures. The method focuses on extreme values of pixelwise statistics rather than averages. ARL is used as a performance measure, with ARL0 set lower than traditional values. The case study involves textile images, but their lack of time-dependency and inconsistent thread positioning may limit applicability. The paper also includes a section on image pre-processing.

This paper contributes to the current literature in several directions. First, we assume that the characteristics of the pixels at a certain time point are not independent as is generally assumed in the literature, but exhibit spatial dependence (see, e.g., Anselin 2010; Elhorst 2010; Cressie and Wikle 2011). To overcome the problem of spatial dependence, we use a spatial covariance matrix, which can be flexibly fixed or estimated from the data. Second, a sequence of images is frequently very persistent in time, and thus exhibits a certain autocorrelation. The pixel characteristics depend not only on the lagged characteristics of the same pixel but also on the lagged characteristics of the neighboring pixels. Therefore, we suggest a spatio-temporal time series model (Cressie and Wikle 2011) to capture this behavior. It is important to note that this is a completely new point that has not been analyzed for image monitoring in the literature up to now.

Since spatio-temporal models are complex and can hardly be handled in higher dimensions, we specify ROIs of a much smaller size that cover the whole image. This method of dimension reduction has been applied to image analysis by several authors

(see, e.g., Megahed et al. 2011, 2012; Okhrin et al. 2020, 2021). The stochastic properties of the characteristics of ROIs are derived directly from the model for the pixels.

In this paper, we introduce several new multivariate control charts for spatio-temporal processes which are based on an EWMA recursion. To overcome the problem of time dependence, some authors have proposed to transform the original data in such a way that the transformed observations are independent. Residual charts are a popular method to monitor time series processes (cf. Alwan and Roberts 1988) but then the problem is how a change influences the residuals, usually a starting problem is available in calculating the residuals and the estimated residuals are no longer independent. A comparison of residual charts and charts directly monitoring the observations, so-called modified charts, is given in Knoth and Schmid (2004). Here we apply such type of residual charts to image processes for the first time and provide an extensive comparison of the newly introduced control charts with their residual counterparts. We calculate the control design and provide several theoretical results, providing a better insight into the behavior of the introduced control procedures. The aim of the schemes is to detect a location shift in the intensity of a grayscale image.

The paper is structured as follows. In Sect. 2 we give a brief introduction to image analysis and statistical image analysis. Here we explain the spatio-temporal model used in the rest of the paper and provide important theoretical results. In Sect. 3 we develop the control charts and discuss the high-dimensional setting of the underlying problem in detail. In Sect. 4, we provide a comparison study of the introduced procedures for several out-of-control situations.

## 2 Model

Let $\mathcal{X}_t = (X_{t,ij})_{i=1,\ldots,r_1,,j=1,\ldots,r_2}$ denote the observed pixel intensities of a rectangular image of size $r_1 \times r_2$. Since noise is always present in the measurement of pixel intensities due to changing environmental influences, the obtained values can be regarded as realizations of a random process. Given that the set of possible colors is very large, we assume that the intensities are continuous random variables. In Okhrin et al. (2020, 2021), grayscale images are considered, and it is assumed that the nominal image is fixed in the in-control state. Moreover, the pixel intensities are assumed to be spatially correlated at a fixed time point but independent across time. In this paper, we relax this restriction.

We assume that the image process is stationary over time. Under this setting, it is possible to describe various dependency structures. For example, if the data follow a *VAR*-type process, then a weak dependence structure is implied. In contrast, assuming a long-memory process results in a strong dependency structure. Note that the stationarity assumption excludes sequences of images, such as movies, from consideration.

Typically, a grayscale image is regarded as a matrix of pixel intensities. Thus, an image process is originally a matrix process over time. However, we can uniquely transform it into a vector process that takes the spatial locations of the pixels into

account. Moreover, the number of pixels is very large in most cases, and therefore, we are confronted with a high-dimensional process.

In the following, the symbols $\mathbb{E}_\infty(.)$, $\mathbb{V}ar_\infty(.)$, and $\mathbb{C}ov_\infty(.)$ denote the mean, variance, and covariance matrix, respectively, computed under the assumption of no change–that is, in the in-control state. The in-control process is denoted by $\mathcal{Y}_t = (Y_{t,ij})\, i = 1, \ldots, r_1, j = 1, \ldots, r_2$. We primarily use the vectorized matrices. The vec operator transforms a matrix into a vector by stacking its columns on top of each other, beginning with the first column, followed by the second column, and so on. Let $\mathrm{X}_t = \text{ vec } (\mathcal{X}_t)$ and $\mathrm{Y}_t = \text{ vec } (\mathcal{Y}_t)$. It is assumed that $\mathbb{E}\infty(\mathrm{X}_t) = \mathbb{E}(\mathrm{Y}_t) = \boldsymbol{\mu}$ and that $\mathbb{C}ov_\infty(\mathrm{X}_{t+h}, \mathrm{X}_t) = \mathbb{C}ov(\mathrm{Y}_{t+h}, \mathrm{Y}_t) = \boldsymbol{\Gamma}(h)$ for any $t$, $h$ in the in-control state.

### 2.1 Modelling the in-control process

For modelling the temporal dependence of $\{\mathcal{Y}_t\}$, matrix-valued time series models as recently proposed by Chen et al. (2021) can be used, i.e.,

$$\mathcal{Y}_t = \mathrm{A}\mathcal{Y}_{t-1}\mathrm{B}' + \mathrm{E}_t.$$

However, the number of parameters is quite high in the high-dimensional case, and the model does not exploit the specific structure of an image process.

Vectorizing $\{\mathcal{Y}_t\}$, we can make use of multivariate time series models, such as the vector autoregressive process

$$\mathrm{Y}_t - \boldsymbol{\mu} = \mathrm{A}(\mathrm{Y}_{t-1} - \boldsymbol{\mu}) + \boldsymbol{\varepsilon}_t, \tag{1}$$

with $\boldsymbol{\varepsilon}_t \sim \mathcal{N}_r(0, \mathrm{G})$. Here, A and G are ($r$, $r$)-matrices with $r = r_1 r_2$, and since $r$ is large, they are difficult to estimate. In order to take the spatial correlation into consideration, the parameter matrices must be chosen in a specific way. Thus, this model suffers from the same disadvantage as the matrix-valued time series model.

Recently, factor models for matrix-valued high-dimensional time series (e.g., Wang et al. 2019; Hallin et al. 2020), i.e.,

$$\mathcal{Y}_t = \boldsymbol{\Lambda}\mathrm{F}_t\mathrm{C}' + \mathrm{E}_t,$$

have been introduced. In this approach, the high-dimensional problem is transformed into a lower-dimensional one. However, since the spatial structure of an image is not considered, we believe that this approach is of limited use in the present case.

In our research study, we want to use approaches that have been used in a similar way in spatial econometrics (see, e.g., LeSage and Pace 2009). Let $\mathrm{W}_i$ denote an arbitrary weight matrix, i.e., all elements of $\mathrm{W}_i$ are non-negative and all values on the main diagonal are equal 0. Note that in applications, $\mathrm{W}_i$ usually depends on certain parameters. We will discuss this point below. Now let

$$\mathrm{Y}_t = \boldsymbol{\mu} + \sum_{i=1}^{p} \mathrm{W}_i(\mathrm{Y}_t - \boldsymbol{\mu}) + \mathrm{A}(\mathrm{Y}_{t-1} - \boldsymbol{\mu}) + \boldsymbol{\varepsilon}_t, \tag{2}$$

where the random vectors $\{\boldsymbol{\varepsilon}_t\}$ are assumed to be independent and identically distributed with mean 0 and covariance matrix G. In this model, the dependence over time is modelled by the autoregressive part and the matrix A controls the influence of past values. The spatial dependence is expressed by the weight matrices and the covariance matrix G. The characteristic of a pixel depends on a linear combination of neighboring pixels. Assuming that the matrix $\mathrm{I} - \sum_{i=1}^{p} \mathrm{W}_i$ has a full rank, we can write (2) as follows

$$\mathrm{Y}_t = \boldsymbol{\mu} + \left(\mathrm{I} - \sum_{i=1}^{p} \mathrm{W}_i\right)^{-1} \mathrm{A}(\mathrm{Y}_{t-1} - \boldsymbol{\mu}) + \left(\mathrm{I} - \sum_{i=1}^{p} \mathrm{W}_i\right)^{-1} \boldsymbol{\varepsilon}_t.$$

Thus, $\{\mathrm{Y}_t\}$ is a *VAR*(1) process. The process is stationary and causal if the absolute values of all eigenvalues of A are smaller than 1. We can show that

$$\mathrm{Y}_t = \boldsymbol{\mu} + \sum_{v=0}^{\infty} \left(\left(\mathrm{I} - \sum_{i=1}^{p} \mathrm{W}_i\right)^{-1} \mathrm{A}\right)^{v} \left(\mathrm{I} - \sum_{i=1}^{p} \mathrm{W}_i\right)^{-1} \boldsymbol{\varepsilon}_{t-v}. \tag{3}$$

For the model (2), we get the autocovariance function given by (cf. Brockwell and Davis 1991)

$$\boldsymbol{\Gamma}(h) = \left((\mathrm{I} - \sum_{i=1}^{p} \mathrm{W}_i)^{-1}\mathrm{A}\right)^{h} \boldsymbol{\Gamma}(0)$$

for $h \geq 1$ and $\boldsymbol{\Gamma}(0)$ is obtained as a solution of the discrete Ljapunov equation (Kitagawa 1977), a special case of the Sylvester equation,

$$\boldsymbol{\Gamma}(0) = \left(\mathrm{I} - \sum_{i=1}^{p} \mathrm{W}_i\right)^{-1} \mathrm{A}\boldsymbol{\Gamma}(0)\mathrm{A}' \left(\mathrm{I} - \sum_{i=1}^{p} \mathrm{W}_i'\right)^{-1} + \left(\mathrm{I} - \sum_{i=1}^{p} \mathrm{W}_i\right)^{-1} \mathrm{G} \left(\mathrm{I} - \sum_{i=1}^{p} \mathrm{W}_i'\right)^{-1}. \tag{4}$$

An analytic solution for $\boldsymbol{\Gamma}_0$ as stated in the next Lemma is crucial for monitoring purposes.

**Lemma 2.1** *The explicit solution of Eq. 4 is given by*

$$vec(\boldsymbol{\Gamma}(0)) = \left((\mathrm{I} - \sum_{i=1}^{p} \mathrm{W}_i) \otimes (\mathrm{I} - \sum_{i=1}^{p} \mathrm{W}_i) - (\mathrm{A} \otimes \mathrm{A})\right)^{-1} vec(\mathrm{G}). \tag{5}$$

Note that although (5) provides an explicit expression of $\mathbf{\Gamma}(0)$, in the high-dimensional case the dimension of the matrices may be huge and the calculation of the inverse matrices may be challenging. Here, the direct procedures for solving the Sylvester equation work much faster (Kitagawa 1977).

### 2.2 Dimension reduction with regions of interest

Since the number of pixels of a digital image is usually huge, we suggest considering subimages—regions of interest (ROI). They are obtained by splitting the original image into disjoint subimages which add up to the whole image. Let $r_1 = \tau_1 l_1$ and $r_2 = \tau_2 l_2$ with natural numbers $\tau_1, \tau_2, l_1, l_2$. Let $\mathcal{Y}_{t,ij} = \left(Y_{t,(i-1)\tau_1+\nu_1,(j-1)\tau_2+\nu_2}\right)_{\nu_1=1,\ldots,\tau_1,\nu_2=1,\ldots,\tau_2}$ then

$$\mathcal{Y}_t = \begin{pmatrix} \mathcal{Y}_{t,11} & \ldots & \mathcal{Y}_{t,1l_2} \\ \ldots & \ldots & \ldots \\ \mathcal{Y}_{t,l_1 1} & \ldots & \mathcal{Y}_{t,l_1 l_2} \end{pmatrix}.$$

Thus the $\mathcal{Y}_{t,ij}$'s, $i = 1, \ldots, l_1, j = 1, \ldots, l_2$ build non-overlapping subimages of $\mathcal{Y}_t$. First, $\{\mathcal{Y}_t\}$ is assumed to be an arbitrary pseudo-image process. In order to reduce the dimension, the characteristics of the subimages are compared with each other. The most popular choice of a characteristic is the mean value of the intensities of the pixels within a subimage. Now, let $\bar{Y}_{t,ij}$ denote the mean value of the subimage $\mathcal{Y}_{t,ij}$, i.e.,

$$\bar{Y}_{t,ij} = \frac{1}{\tau_1\tau_2} \sum_{\nu_1=1}^{\tau_1} \sum_{\nu_2=1}^{\tau_2} Y_{t,(i-1)\tau_1+\nu_1,(j-1)\tau_2+\nu_2} = \frac{1}{\tau_1\tau_2} 1'_{\tau_1} \mathcal{Y}_{t,ij} 1_{\tau_2}.$$

Then we define $\bar{\mathcal{Y}}_t = (\bar{Y}_{t,ij})_{i=1,\ldots,l_1 j=1,\ldots,l_2}$. Suppose next that the mean process $\{\text{ vec }(\bar{\mathcal{Y}}_t)\}$ satisfies the Eq. (2). Is it possible to construct an original process $\{\mathcal{Y}_t\}$ which fulfils (2) as well? In principle, it can be expected that the process possesses this property since the weights of the mean process only fix the relationship between the rectangles and there is still a lot of freedom to choose the weights for the individual pixels. This problem is discussed in full detail in Okhrin et al. (2025). The main result is summarized in Theorem 2.2.

**Theorem 2.2** *Let $\{\mathcal{Y}_t\}$ denote an image process and $\{\bar{\mathcal{Y}}_t\}$ its mean process as defined above. Suppose that the mean process is a spatial process which fulfils (2). Then there exists an image process $\{\mathcal{Y}_t\}$ which satisfies (2) as well and it has the same order as its mean process.*

Note that a weight matrix W is a $r_1 r_2 \times r_1 r_2$-matrix. Let $w_{ij,v\mu}$ correspond to the weight related to the pixel points at positions $(i, j)$ and $(v, \mu)$. If, e.g., $r_1 = 2$ and $r_2 = 3$ then

$$\mathrm{W} = \left(\begin{array}{cc|cc|cc} w_{11,11} & w_{21,11} & w_{12,11} & w_{22,11} & w_{13,11} & w_{23,11} \\ w_{11,21} & w_{21,21} & w_{12,21} & w_{22,21} & w_{13,21} & w_{23,21} \\ \hline w_{11,12} & w_{21,12} & w_{12,12} & w_{22,12} & w_{13,12} & w_{23,12} \\ w_{11,22} & w_{21,22} & w_{12,22} & w_{22,22} & w_{13,22} & w_{23,22} \\ \hline w_{11,13} & w_{21,13} & w_{12,13} & w_{22,13} & w_{13,13} & w_{23,13} \\ w_{11,23} & w_{21,23} & w_{12,23} & w_{22,23} & w_{13,23} & w_{23,23} \end{array}\right) = \left(\begin{array}{ccc} \mathrm{W}_{11} & \mathrm{W}_{12} & \mathrm{W}_{13} \\ \mathrm{W}_{21} & \mathrm{W}_{22} & \mathrm{W}_{23} \\ \mathrm{W}_{31} & \mathrm{W}_{32} & \mathrm{W}_{33} \end{array}\right).$$

In general, we have that $\mathrm{W}_{j\mu} = (w_{i\mu,vj})_{v=1,..,r_1,i=1,..,r_1}$ for $j, \mu \in \{1, .., r_2\}$. Now if, e.g., W is the 1-nearest neighbor matrix, i.e. $w_{i\mu,vj} = 1$ if $(i-v)^2 + (j-\mu)^2 = 1$, else 0, then we get for the above case that

$$\mathrm{W} = \left(\begin{array}{cc|cc|cc} 0 & 1 & 1 & 0 & 0 & 0 \\ 1 & 0 & 0 & 1 & 0 & 0 \\ \hline 1 & 0 & 0 & 1 & 1 & 0 \\ 0 & 1 & 1 & 0 & 0 & 1 \\ \hline 0 & 0 & 1 & 0 & 0 & 1 \\ 0 & 0 & 0 & 1 & 1 & 0 \end{array}\right).$$

We see that $W_{j\mu} = 0$ if $|j - \mu| \geq 2$. In the case of a $\tau$-nearest neighbor matrix, it holds that $W_{j\mu} = 0$ if $|j - \mu| \geq \tau + 1$. Thus, a lot of the blocks are equal to zero, which simplifies the practical analysis.

In practice, the weight matrix usually depends on some parameters. This makes their application more attractive. The easiest approach is to assume a multiplicative factor. In that case, it holds that $\mathrm{W}_i = \delta_i \mathrm{W}_i^*$ with $\delta_i \in (0, 1)$. $\mathrm{W}_i^*$ is a weight matrix as described above which in most cases is also assumed to be row-standardized, i.e. the sum of the elements of a row is equal to 1.

This approach seems to be simple and natural. However, the variety of possible images is huge, and this model provides only a first step. It can be generalized easily by allowing $\delta$'s to change over time, e.g., assuming $(\delta_{t1}, \ldots, \delta_{tp})$ follows a *VAR*(1) process. Then, we would have one non-observable process, as in the case of Kalman filters. We will not discuss such attempts here and focus on the discussion of the model (2).

The disadvantage of this approach is that the $\delta_{ti}$'s do not depend on the specific spatial point of the image and are the same for all points. Models where the transition of a pixel from a time point to the next is explained in an individual way seem to be quite complicated. Here a Bayesian approach could be useful. This will be a topic of future research.

### 2.3 Modelling the out-of-control process

The number of possible disturbances in real images is vast. In our paper, we focus on changes in the pixel intensities. We make use of the following change point model for $t \geq 1$

$$\mathrm{X}_t = \begin{cases} \mathrm{Y}_t + \mathrm{a} & \text{for} \quad t \geq \tau \\ \mathrm{Y}_t & \text{for} \quad t < \tau \end{cases} \tag{6}$$

where $\mathrm{a} \in \mathbb{R}^r - \{0\}$ and $\tau \in \{1, 2, \ldots, \infty\}$. We say that the observed process is in-control if $\tau = \infty$, else it is said to be out-of-control. The model implies that the change influences the mean behavior of the pixel intensities. It holds that $\mathbb{E}(\mathrm{X}_t) = \boldsymbol{\mu}$ for $t < \tau$, $\mathbb{E}(\mathrm{X}_t) = \boldsymbol{\mu} + \mathrm{a}$ for $t \geq \tau$, and $\mathbb{C}ov(\mathrm{X}_{t+h}, \mathrm{X}_h) = \boldsymbol{\Gamma}(h)$.

Note, that intensities in image analysis are standardized to the unit interval. Both in the in-control or out-of-control states, the simulated intensities may fall outside the interval and render false images. This problem can be handled either by manual constraining of the values or by choosing small variances of the residuals and, thus, making the probability of large or negative values of the intensities negligible.

## 3 EWMA type control statistics

In this section, we consider several multivariate control charts for the mean, which are based on exponentially weighted moving average (EWMA) recursions. It is assumed that $\{\mathrm{Y}_t\}$ is a stationary process with mean $\boldsymbol{\mu}$ and cross-covariance matrices $\boldsymbol{\Gamma}(h)$.

### 3.1 The multivariate EWMA chart for time series

Kramer and Schmid (1997) extended the multivariate EWMA control chart of Lowry et al. (1992) for independent samples to time series. Let

$$\mathrm{Z}_t = (\mathrm{I} - \boldsymbol{\Lambda})\mathrm{Z}_{t-1} + \boldsymbol{\Lambda}\mathrm{X}_t, \quad t \geq 1, \tag{7}$$

where $\mathrm{Z}_0 = \boldsymbol{\mu}$, $\boldsymbol{\Lambda} = diag(\lambda_1, \ldots, \lambda_r)$ with $\lambda_1, \ldots, \lambda_r \in (0, 1]$. Rewriting (7) we get

$$\mathrm{Z}_t - \boldsymbol{\mu} = (\mathrm{I} - \boldsymbol{\Lambda})(\mathrm{Z}_{t-1} - \boldsymbol{\mu}) + \boldsymbol{\Lambda}(\mathrm{X}_t - \boldsymbol{\mu}), \quad t \geq 1$$

and thus for $t \geq 1$ we obtain

$$\mathrm{Z}_t = \boldsymbol{\mu} + \boldsymbol{\Lambda} \sum_{i=0}^{t-1} (\mathrm{I} - \boldsymbol{\Lambda})^i (\mathrm{Y}_{t-i} - \boldsymbol{\mu}) + \boldsymbol{\Lambda} \sum_{i=0}^{t-\tau} (\mathrm{I} - \boldsymbol{\Lambda})^i \mathrm{a}. \tag{8}$$

According to Kramer and Schmid (1997), we get for *r* fixed that

$$\mathbb{E}(\mathrm{Z}_t) = \boldsymbol{\mu} + (\mathrm{I} - (\mathrm{I} - \boldsymbol{\Lambda})^{t-\tau+1})\mathrm{a} I_{\{\tau, \tau+1, \ldots\}}(t)$$

and

$$\begin{aligned} \mathbb{C}ov(\mathrm{Z}_t) =& \boldsymbol{\Lambda} \sum_{i,j=0}^{t-1} (\mathrm{I} - \boldsymbol{\Lambda})^i \boldsymbol{\Gamma}(j-i)(\mathrm{I} - \boldsymbol{\Lambda})^j \boldsymbol{\Lambda} \\ \rightarrow & \boldsymbol{\Lambda} \sum_{i,j=0}^{\infty} (\mathrm{I} - \boldsymbol{\Lambda})^i \boldsymbol{\Gamma}(j-i)(\mathrm{I} - \boldsymbol{\Lambda})^j \boldsymbol{\Lambda} \end{aligned}$$

as $t \to \infty$, provided that $\{\mathbf{\Gamma}(v)\}$ is absolutely summable, i.e. that $\sum_{v=0}^{\infty} ||\mathbf{\Gamma}(v)|| < \infty$.

Now let

$$\mathbf{\Sigma}_{t,r} = \mathbb{C}ov_{\infty}(\mathrm{Z}_t), \quad \mathbf{\Sigma}_{l;r} = \lim_{t\to\infty} \mathbb{C}ov_{\infty}(\mathrm{Z}_t) = \mathbf{\Lambda} \sum_{i,j=0}^{\infty} (\mathrm{I} - \mathbf{\Lambda})^i \mathbf{\Gamma}(j-i)(\mathrm{I} - \mathbf{\Lambda})^j \mathbf{\Lambda}. \quad (9)$$

$\mathbf{\Sigma}_{l;r}$ denotes the limit of the covariance matrix of $\mathrm{Z}_t$ as $t \to \infty$ and $r$ is fixed.

The MEWMA chart is based on the Mahalanobis distance between $\mathrm{Z}_t$ and its expected value in the in-control case. This leads to

$$T_{1,t,r} = (\mathrm{Z}_t - \boldsymbol{\mu})' \mathbf{\Sigma}_{t,r}^{-1} (\mathrm{Z}_t - \boldsymbol{\mu}).$$

Frequently, the asymptotic covariance matrix is used instead of the exact one. This procedure has the advantage that the inverse matrix has to be determined only once and not for every time period. In the high-dimensional case, this property is of great advantage. Thus, we obtain

$$T_{2,t,r} = (\mathrm{Z}_t - \boldsymbol{\mu})' \mathbf{\Sigma}_{l;r}^{-1} (\mathrm{Z}_t - \boldsymbol{\mu}).$$

Kramer and Schmid (1997) proposed these control procedures. They analyzed under what conditions the resulting charts are directionally invariant. Bodnar et al. (2023) derived several distributional properties of these statistics. Among others, the first two moments in the out-of-control state are given. In the following, we will make use of some of these results, and we derive further properties of the applied control statistics. These results are summarized in Lemmas 6.1 and 6.2 of the appendix.

Now, our control statistics are obtained by normalizing $T_{i,t,r}$, $i = 1, 2$. Using Lemma 6.1 we get

$$CS_{1,t,r} = \frac{T_{1,t,r} - r}{\sqrt{2r}} \qquad \text{and} \qquad CS_{2,t,r} = \frac{T_{2,t,r} - \mathrm{tr}(\mathbf{\Sigma}_{l;r}^{-1} \mathbf{\Sigma}_{t,r})}{\sqrt{2\mathrm{tr}((\mathbf{\Sigma}_{l;r}^{-1} \mathbf{\Sigma}_{t,r})^2)}}. \quad (10)$$

The corresponding control charts give a signal at a time point $t$ if the control statistics are sufficiently large. The run lengths of these schemes are

$$N_i = \inf\{t \in \mathbb{N} : CS_{i,t,r} > c_i\}$$

for $i = 1, 2$ where $c_1$ and $c_2$ denote suitable constants. In industrial engineering, the constants are frequently chosen to be 3. This is motivated by the case of independent Shewhart-type control statistics where for $\tau = 1$ the expected run length is equal to the inverse of the power function and $3\sigma$ intervals are chosen. For dependent control statistics, the situation is more complicated. There are only explicit expressions for the ARL for special cases (e.g., Schmid 1995). Usually, Monte Carlo simulations are used to estimate the ARL and the control limits $c_i$ are taken such that the sample in-control ARL is equal to a pre-specified value, say $\xi$. The value of $\xi$ depends on

the amount of observations. It says that on average a false decision is made after $\xi$ observations because it is concluded that the process is out-of-control while it is in-control in reality. The in-control ARL0 is usually determined either for computational convenience or based on a specific application. An ARL0 of 370 corresponds to the critical value $c = 3$ for the Shewhart control chart. In engineering as common value is 500; in finance, common choices include 60, 120, or 250, reflecting three, six, or twelve months of trading data.

Since the first two moments of $T_{1,t,r}$ do not depend on $t$, the normalization in (10) does not influence the stochastic properties of the corresponding control charts. It is not necessary to normalize in this case. The advantage of doing this is to make use of the asymptotic normality of the normalized quantities and thus, to get $3\sigma$ control limits which are comparable with that of a normal sample. In contrast, normalizing $T_{2,t,r}$ is important, since both the first and the second moment depend on $t$.

Now let

$$\begin{aligned} \mathrm{a}_{t-\tau} &= (\mathrm{I} - (\mathrm{I} - \mathbf{\Lambda})^{t-\tau+1})\mathrm{a} I_{\{0,1,2\ldots\}}(t-\tau), \\ \zeta_{\tau,t,r} &= \mathrm{a}'_{t-\tau}\mathbf{\Sigma}^{-1}_{t,r}\mathrm{a}_{t-\tau}, \quad \zeta_{l;\tau,r} = \mathrm{a}'\mathbf{\Sigma}^{-1}_{l;r}\mathrm{a}\, I_{\mathbb{N}}(\tau). \end{aligned} \tag{11}$$

Note that both non-centrality parameters are non-decreasing in $\mathrm{a}$ and they are equal to zero if there is no change.

Lemma 6.1 shows that

$$\mathbb{E}(CS_{1,t,r}) = \frac{\zeta_{\tau,t,r}}{\sqrt{2r}}, \quad \mathbb{V}ar(CS_{1,t,r}) = 1 + 2\frac{\zeta_{\tau,t,r}}{r} = 1 + 2^{3/2}\frac{\mathbb{E}(CS_{1,t,r})}{\sqrt{r}}.$$

Consequently, the change influences both the mean and the variance of the control statistic $CS_{1,t,r}$. The expectation and the variance are getting larger if a change is present. We also see that the change influences more the mean than the variance.

Further, Lemma 6.1b) shows that for $t$ and $r$ large the distribution of $CS_{1,t,r}$ behaves approximately as

$$N\left(\frac{\zeta_{l;\tau,r}}{\sqrt{2r}}, 1 + 2\frac{\zeta_{l;\tau,r}}{r}\right). \tag{12}$$

Here we also see the influence of $r$. However, the asymptotic behavior is questionable since in our applications $r$ is large but $t$ may be relatively small. Thus, it is of interest to know the asymptotic behavior as $r$ goes to infinity and $t$ is fixed. Lemma 6.1c) shows that the asymptotic distribution of $CS_{1,t,r}$ is

$$N\left(\frac{\zeta_{\tau,t,r}}{\sqrt{2r}}, 1 + 2\frac{\zeta_{\tau,t,r}}{r}\right). \tag{13}$$

It is not the same as in (12) if a change is present, since for $t$ fixed $\zeta_{\tau,t,r} - \zeta_{l;\tau,r}$ does not converge to zero as $r$ tends to infinity. Thus, the asymptotic (12) should not be

applied in that case. Summarizing, we can state that the control chart $CS_{1,t,r}$ works well with the approximation (13).

The situation is slightly different for $CS_{2,t,r}$. On the one side, it holds that for $r$ fixed $\operatorname{tr}(\boldsymbol{\Sigma}_{l;\tau,r}^{-1}\boldsymbol{\Sigma}_{\tau,t,r}) \to r$ and $\operatorname{tr}((\boldsymbol{\Sigma}_{l;\tau,r}^{-1}\boldsymbol{\Sigma}_{\tau,t,r})^2) \to r$ as $t$ goes to infinity. On the other side, this is not the case if $t$ is fixed and $r$ goes to infinity. Because of Lemma 6.1e) and f) the control statistic with the exact in-control means must be used as defined in (10).

Comparing $CS_{1,t,r}$ and $CS_{2,t,r}$, we see that the calculations with $T_{2,t,r}$ are easier, since the inverse of the covariance matrix must be calculated only once. To compute $CS_{2,t,r}$ we need the first two in-control moments that depend on $t$ and, therefore, we have to determine an inverse matrix for each $t$. Thus, the effort of calculating both control charts is comparable and none of the charts dominates concerning this criteria.

Further, we see that if $\lim_{r\to\infty} \frac{\zeta_{\tau,t,r}}{\sqrt{2r}} = 0$, i.e., if for instance $\zeta_{\tau,t,r}$ is bounded, the change disappears asymptotically. Therefore, a change in one or a few components will be difficult to detect in a high-dimensional environment. The same holds for the chart based on the asymptotic variance.

Next, we analyze the results for model (2). Note that $\{\mathrm{Y}_t\}$ is a VAR(1) process. Further, it is assumed that $\boldsymbol{\Lambda} = \lambda\mathrm{I}$ with $\lambda \in (0, 1]$. This assumption is often made in applications to reduce the amount of smoothing parameters. It follows with remark b) to Theorem 1 of Kramer and Schmid (1997) that with $\boldsymbol{\Phi} = (\mathrm{I} - \sum_{i=1}^{p} \delta_i \mathrm{W}_i)^{-1}\mathrm{A}$

$$
\begin{aligned}
\boldsymbol{\Sigma}_{t,r} =& \lambda^2 \sum_{i=0}^{t-1} \sum_{v=0}^{t-1-i} (1-\lambda)^{i+2v} \boldsymbol{\Phi}^i \boldsymbol{\Gamma}(0) + \lambda^2 \boldsymbol{\Gamma}(0) \sum_{i=1}^{t-1} \sum_{v=i}^{t-1} (1-\lambda)^{-i+2v} (\boldsymbol{\Phi}')^i \\
=& \frac{\lambda}{2-\lambda} \left[ (\mathrm{I} - (1-\lambda)\boldsymbol{\Phi})^{-1} (\mathrm{I} - (1-\lambda)^t \boldsymbol{\Phi}^t) \right. \\
& \left. - (1-\lambda)^{2t} (\mathrm{I} - (1-\lambda)^{-1}\boldsymbol{\Phi})^{-1} (\mathrm{I} - (1-\lambda)^{-t}\boldsymbol{\Phi}^t) \right] \boldsymbol{\Gamma}(0) \\
& + \frac{\lambda}{2-\lambda} \boldsymbol{\Gamma}(0) \left[ -(1-\lambda)^{2t} (\mathrm{I} - (1-\lambda)^{-1}\boldsymbol{\Phi}')^{-1} (\mathrm{I} - (1-\lambda)^{-t}\boldsymbol{\Phi}'^t) \right. \\
& \left. + (\mathrm{I} - (1-\lambda)\boldsymbol{\Phi}')^{-1} (\mathrm{I} - (1-\lambda)^t \boldsymbol{\Phi}'^t) \right] - \frac{\lambda}{2-\lambda} \boldsymbol{\Gamma}(0)(1 - (1-\lambda^{2t}))
\end{aligned}
$$

and

$$
\boldsymbol{\Sigma}_{l;r} = \frac{\lambda}{2-\lambda} \left( (\mathrm{I} - (1-\lambda)\boldsymbol{\Phi})^{-1} \boldsymbol{\Gamma}(0) + \boldsymbol{\Gamma}(0)(\mathrm{I} - (1-\lambda)\boldsymbol{\Phi}')^{-1} - \boldsymbol{\Gamma}(0) \right)
$$

using that $\sum_{i=0}^{t-1} \mathrm{B}^i = (\mathrm{I} - \mathrm{B})^{-1}(\mathrm{I} - \mathrm{B}^t)$ and provided that the inverse of $\mathrm{I} - \mathrm{B}$ exists. Note that an explicit expression for $\boldsymbol{\Gamma}(0)$ is given in (5). This shows that both $\boldsymbol{\Sigma}_{t,r}$ and $\boldsymbol{\Sigma}_{l;r}$ can be explicitly calculated if G and $\boldsymbol{\Phi}$ are known. Nevertheless, it is necessary to determine the inverse of high-dimensional matrices for the calculation of $CS_{1,t,r}$ and $CS_{2,t,r}$ which may be a problem for large $r$.

### 3.2 A control approach based on the euclidean distance of the EWMA recursions

Next, we use as a control statistic the Euclidean distance between $\mathrm{Z}_t$ and its in-control mean, i.e.,

$$(\mathrm{Z}_t - \boldsymbol{\mu})'(\mathrm{Z}_t - \boldsymbol{\mu})$$

for $t \geq 1$. The great advantage of this quantity compared to the control statistic based on the Mahalanobis distance is that it does not depend on the inverse covariance matrix and, therefore, is much easier to calculate.

Motivated by the papers of Bai and Saranadasa (1996), Chen and Qin (2010), Okhrin et al. (2020) and Okhrin et al. (2021) introduced two control charts for monitoring independent image processes based on the Euclidean distance. Bodnar et al. (2023) considered an EWMA chart based on the Euclidean distance for multivariate time series. Next, we want to analyze the performance of their approach for monitoring image processes. We make use of Lemma 6.2 of the Appendix, where some results of Bodnar et al. (2023) together with some new results are summarized.

We normalize the Euclidean distance by its first two in-control moments (see Lemma 6.2) and get

$$CS_{3,t,r} = \frac{(\mathrm{Z}_t - \boldsymbol{\mu})'(\mathrm{Z}_t - \boldsymbol{\mu}) - \operatorname{tr}(\boldsymbol{\Sigma}_{t,r})}{\sqrt{2 \operatorname{tr}(\boldsymbol{\Sigma}_{t,r}^2)}}. \tag{14}$$

Bodnar et al. (2023) proved that in the in-control state the control statistic $CS_{3,t,r}$ is asymptotically standard normally distributed if $t$ is fixed and $r$ converges to infinity (cf. Lemma 6.2).

Note that replacing $\boldsymbol{\Sigma}_{t,r}$ by $\boldsymbol{\Sigma}_{l;r}$ in (14) does not change its asymptotic behavior if $r$ and $t$ converge to infinity (Lemma 6.2c), second part), but it does in the case that $r$ is fixed and $t$ tends to infinity (cf. Lemma 6.2c), first part).

Following Lemma 6.2d), $CS_{3,t,r}$ behaves asymptotically for $t$ fixed and $r$ tending to infinity as

$$N\left(\frac{\mathrm{a}_{t-\tau}'\mathrm{a}_{t-\tau}}{\sqrt{2\mathrm{tr}(\boldsymbol{\Sigma}_{t,r}^2)}}, 1 + 2\frac{\mathrm{a}_{t-\tau}'\boldsymbol{\Sigma}_{t,r}\mathrm{a}_{t-\tau}}{\mathrm{tr}(\boldsymbol{\Sigma}_{t,r}^2)}\right). \tag{15}$$

Note that to calculate $C_{3,t,r}$ only the traces of $\boldsymbol{\Sigma}_{t,r}$ and $\boldsymbol{\Sigma}_{t,r}^2$ must be known. Nevertheless, we need to know these quantities for all values of $t$. Equation (15) illustrates how a influences the speed of change detection. The change influences the mean and the variance of the asymptotic distribution.

### 3.3 Residual charts

Residual charts are based on a transformation of the original data. The aim is to get new quantities that are independent in the in-control state. Then all the classical control procedures can be applied to these residuals. Residual charts were originally proposed by Alwan and Roberts (1995). A general discussion of this approach is given in Okhrin and Schmid (2007). Since the residuals can be easily recursively calculated for stationary processes (cf. Brockwell and Davis 1991), this approach is very useful for this data type. A disadvantage of this approach lies in the fact that the original data are transformed and thus changes in the transformed variables are detected. There are several comparisons of the residual charts with the modified chart, i.e., charts which are obtained by extending the classical charts for independent variables taking into account the time series structure (e.g., Schmid 1997; Knoth and Schmid 2004).

Suppose that the process $\{\mathrm{Y}_t\}$ is stationary with mean $\boldsymbol{\mu}$. Let $\hat{\mathrm{Y}}_t$ be the best linear 1-step predictor of $\mathrm{Y}_t$ given $\mathrm{Y}_{t-1}$,..., $\mathrm{Y}_1, 1$. Then $\hat{\mathrm{Y}}_t = \boldsymbol{\mu} + \sum_{v=1}^{t-1} \mathrm{A}_{vt}\mathrm{Y}_{t-v}$ with certain matrices $\mathrm{A}_{vt}$, $v = 1, \ldots, t-1$( cf. Brockwell and Davis 1991). Now let $\hat{\mathrm{X}}_t = \boldsymbol{\mu} + \sum_{v=1}^{t-1} \mathrm{A}_{vt}\mathrm{X}_{t-v}$, i.e., $\hat{\mathrm{X}}_t$ is equal to $\hat{\mathrm{Y}}_t$ in the in-control state. Then normalized residuals are given by

$$\boldsymbol{\eta}_t = (\mathbb{C}ov_\infty(\mathrm{X}_t - \hat{\mathrm{X}}_t))^{-1/2}(\mathrm{X}_t - \hat{\mathrm{X}}_t).$$

They are independent in the in-control state with $\boldsymbol{\eta}_t \sim \mathcal{N}_r(0, \mathrm{I})$. Consequently, all the previous results of this paper can be applied to the residuals by replacing $\mathrm{X}_t$ by $\boldsymbol{\eta}_t$.

If we apply the EWMA recursion (7) to the residuals $\{\boldsymbol{\eta}_t\}$, then we denote the EWMA statistic by $\mathrm{Z}_t^{(r)}$ and the components of $\mathrm{vec}(\mathrm{Z}_t)$ by $Z_{ti}^{(r)}$. The upper index $r$ is also used for the covariance matrices in (9). We obtain that

$$\boldsymbol{\Sigma}_{l,r}^{(r)} = \boldsymbol{\Lambda}(\mathrm{I} - (\mathrm{I} - \boldsymbol{\Lambda})^2)^{-1}\boldsymbol{\Lambda} = \boldsymbol{\Lambda}(2\mathrm{I} - \boldsymbol{\Lambda})^{-1}, \qquad \boldsymbol{\Sigma}_{t,r}^{(r)} = \boldsymbol{\Lambda}(2\mathrm{I} - \boldsymbol{\Lambda})^{-1}(\mathrm{I} - (\mathrm{I} - \boldsymbol{\Lambda})^{2t}).$$

Thus, the residual charts based on $C_{1,t,r}$, $C_{2,t,r}$, and $C_{3,t,r}$ have the control statistics

$$CS_{1,t,r}^{(r)} = \frac{\sum_{i=1}^{r} \frac{2-\lambda_i}{\lambda_i\,(1-(1-\lambda_i)^{2t})}\, {Z_{ti}^{(r)}}^2 - r}{\sqrt{2r}},$$

$$CS_{2,t,r}^{(r)} = \frac{\sum_{i=1}^{r} \frac{2-\lambda_i}{\lambda_i} {Z_{ti}^{(r)}}^2 - \sum_{i=1}^{r}(1-(1-\lambda_i)^{2t})}{\sqrt{2\sum_{v=1}^{r}(1-(1-\lambda_v)^{2t})^2}},$$

$$CS_{3,t,r}^{(r)} = \frac{\sum_{i=1}^{r} {Z_{ti}^{(r)}}^2 - \sum_{i=1}^{r}(1-(1-\lambda_i)^{2t})\,\frac{\lambda_i}{2-\lambda_i}}{\sqrt{2\sum_{i=1}^{r}\frac{\lambda_i^2}{(2-\lambda_i)^2}(1-(1-\lambda_i)^{2t})^2}}.$$

In applications, frequently the matrix $\mathbf{\Lambda}$ is chosen as a diagonal matrix to reduce the amount of smoothing parameters, i.e., $\mathbf{\Lambda} = \lambda \mathrm{I}$ with $\lambda \in (0, 1]$. Note that in this case we have that $CS^{(r)}_{1,t,r} = CS^{(r)}_{2,t,r} = CS^{(r)}_{3,t,r}$.

Since the residuals are independent, it is also possible to apply the charts proposed in Okhrin et al. (2020) and Okhrin et al. (2021) to the residual process. Using the notation of Okhrin et al. (2021), we denote the residual control statistics based on $R_n$, $M_n$, and $U_n$ by $CS^{(r)}_{4,t,r}$, $CS^{(r)}_{5,t,r}$, and $CS^{(r)}_{6,t,r}$. A chart gives a signal at time $t$ if $CS_{i,t,r}$ is sufficiently large.

Thus, the control design is on the one side simpler. However, in order to obtain $\hat{\mathrm{X}}_t$, we have to fix a certain model for $\mathrm{X}_t$ in the in-control case and to determine $\mathbb{C}ov_\infty(\mathrm{X}_t - \hat{\mathrm{X}}_t)$. In the present case, i.e., model (2), the predictor is given by (cf. Brockwell and Davis 1991)

$$\hat{\mathrm{X}}_t = \begin{cases} \boldsymbol{\mu} + (\mathrm{I} - \sum_{i=1}^{p} \delta_i \mathrm{W}_i)^{-1} \mathrm{A}(\mathrm{X}_{t-1} - \boldsymbol{\mu}) & \text{for} \quad t \geq 2 \\ \boldsymbol{\mu} & \text{for} \quad t = 1 \end{cases} .$$

The in-control prediction error is equal to

$$\mathbb{C}ov_\infty(\mathrm{X}_t - \hat{\mathrm{X}}_t) = \begin{cases} (\mathrm{I} - \sum_{i=1}^{p} \delta_i \mathrm{W}_i)^{-1} \mathrm{G} (\mathrm{I} - \sum_{i=1}^{p} \delta_i \mathrm{W}_i')^{-1} & \text{for} \quad t \geq 2 \\ \mathbf{\Gamma}(0) & \text{for} \quad t = 1 \end{cases} .$$

Note that the parameters of the underlying spatial time series model are unknown and must be estimated in practice. This leads to two critical problems. First, disentangling the spatial and temporal components given by matrices $W_i$ and $A$ is computationally and technically demanding (LeSage and Pace 2009). Second, the estimation risk influences the performance of the monitoring schemes. In the context of quality control, this problem has been studied by several authors for independent samples (e.g., Jensen et al. 2006; Psarakis et al. 2014; Does et al. 2022) but there are only a few papers dealing with univariate time series (e.g., Kramer and Schmid 2000; Garza-Venegas et al. 2018). Recently, Bodnar et al. (2024) studied the influence of parameter estimation on high-dimensional time series. The impact of the misspecification on the performance was analyzed analytically and with simulation. A similar analysis within the context of the spatial model considered in this paper is left for future research.

## 4 Simulation study

In the presented simulation study, *the proposed analysis method* starts with selecting a nominal image and partitioning it into ROIs. Parameters for the spatial vector autoregressive process are then specified, enabling the simulation of an in-control process. Control limits for the proposed control charts are determined, ensuring the same in-control average run length $(ARL_0)$. Subsequently, different change scenarios are introduced for the out-of-control case. The performance of the control charts is evaluated by their capacity to quickly detect the changes, corresponding ARLs are

then summarized in a table. This is followed by a result analysis together with some recommendations for the practitioners. Each step is elaborated upon in detail in the following portions of this section.[1]

We start the analysis by assuming an already *pre-processed image*, meaning there is no need to adjust positioning or lighting. For this study, we consider a real photo of size $300 \times 300$ pixels as shown in Fig. 1 (left) and normalize the values of pixel intensities to be between 0 and 1. The picture is then divided into ROIs of size $20 \times 20$ pixels, resulting in $15 \times 15$ non-overlapping ROIs. We characterize each region of interest by the average intensity of pixels contained in the corresponding ROI (Fig. 1, right). This matrix of values is rearranged in a vector and will be further used for simulations.

The next step is to specify *parameters* for the spatial vector autoregressive process of order 1 model (2). The in-control mean $\boldsymbol{\mu}_0$ equals the vectorized matrix of expected ROI characteristics. The weight matrix is chosen to be $\mathrm{W}_1 = \delta_1 \mathrm{W}_1^*$, the matrix A is a diagonal matrix with all diagonal elements equal 0.5, i.e., $\mathrm{A} = \mathrm{diag}_{r\times r}(0.5)$, and $\mathrm{G} = \mathrm{diag}_{r\times r}(0.005^2)$. The matrix $\mathrm{W}_1^*$ is taken as a normalized nearest neighbor matrix. Its entries are equal to 1 if the Euclidean distance between the coordinates of the neighboring pixels is less than $\sqrt{18}$, else the value is 0. Further, the matrix is normalized such that all row sums are equal to 1. Note that the choice of parameters is crucial for the stationarity of the spatial temporal process. Following Ekström and Serra-Capizzano (2018) (Eq. 9), we can guarantee that the eigenvalues of the process are less than one by choosing a suitable factor $\delta_1$. Here we set $\delta_1 = 0.01$.

Now, a sequence of time-dependent values can be generated (by using the model (2), which represents the *in-control process*. The images in Fig. 2 illustrate the result-

[1] The R code is available at https://github.com/ViktoriiaPetruk/Monitoring-Time-Dependent-Image-Proce

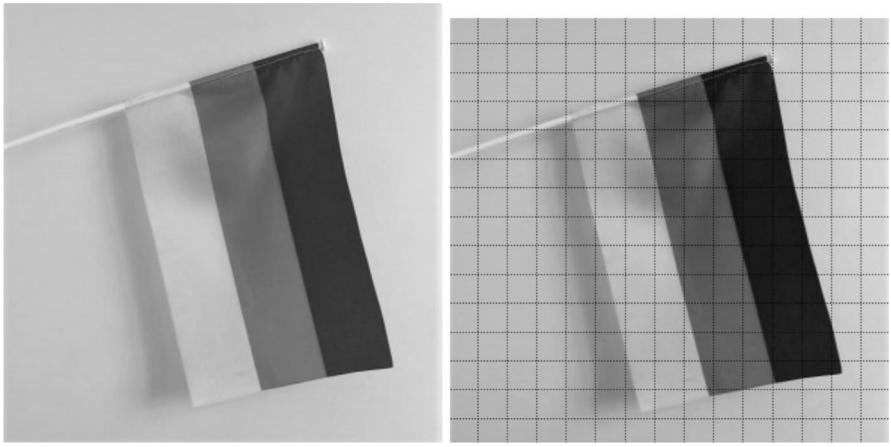

**Fig. 1** Original image $300 \times 300$ pixels (left) and $15 \times 15$ non-overlapping ROIs $20 \times 20$ pixels each (right)

sses-for-Detecting-Shifts-in-Pixel-Intensities.

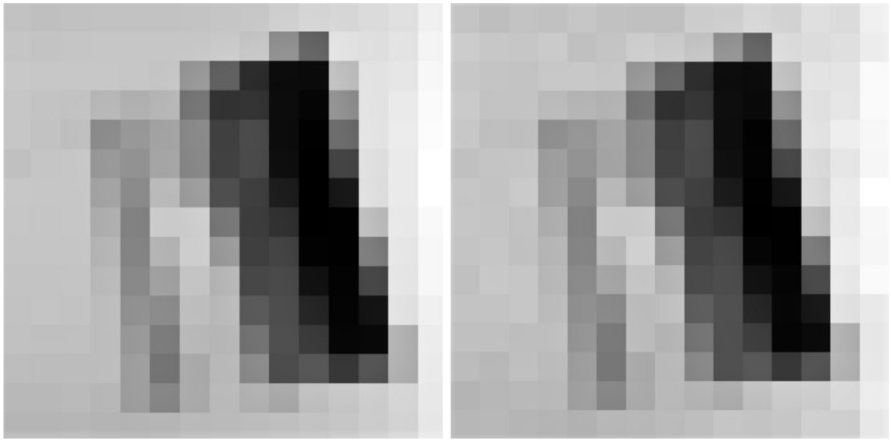

**Fig. 2** Visualisation of $15 \times 15$ non-overlapping ROI characteristics (left) and one of the steps of the in-control process simulation with noise (right)

**Table 1** Control limits of the control statistics $CS_{1,t,r}$, $CS_{2,t,r}$, $CS_{3,t,r}$ and $CS^{(r)}_{3,t,r}$ for different values of the smoothing parameter $\lambda$ for an in-control $ARL = 100$

| | $\lambda = 0.2$ | $\lambda = 0.5$ | $\lambda = 0.8$ | $\lambda = 1.0$ |
|---|---|---|---|---|
| $CS_{1,t,r}$ | 2.112586 | 2.337000 | 2.416760 | 2.442373 |
| $CS_{2,t,r}$ | 2.113669 | 2.341900 | 2.417600 | 2.447500 |
| $CS_{3,t,r}$ | 2.111868 | 2.339200 | 2.417677 | 2.446350 |
| $CS^{(r)}_{3,t,r}$ | 2.272030 | 2.430834 | 2.458000 | 2.465000 |

ing ROI image and its noisy version during the in-control generating procedure. A closer look reveals vague differences in the brightness of the corresponding ROIs due to the noise in the data-generating process.

To compare the performance of the proposed control charts, i.e. the charts based on the original values $CS_{1,t,r}$, $CS_{2,t,r}$, $CS_{3,t,r}$ and the residual chart $CS^{(r)}_{3,t,r}$( Note that in the present case it holds that $CS^{(r)}_{1,t,r} = CS^{(r)}_{2,t,r} = CS^{(r)}_{3,t,r}$) the ARL: $E[RL(c)]$ is used as a performance measure, where the run length is defined as

$$RL(c) = \inf\{t \in \mathbb{N} : |CS_{\cdot,t,\cdot}| > c\}, \tag{16}$$

where $c$ is the control limit. To reduce the number of parameters, we assume equal smoothing parameters, i.e. the diagonal elements of the weight matrix $\mathbf{\Lambda}$ are $\lambda_i = \lambda$ for $i = 1, \ldots, r$. Here $\lambda \in \{0.2,\ 0.5,\ 0.8,\ 1.0\}$( i.e., $\mathbf{\Lambda} = \lambda \mathrm{I}_{r\times r}$) to reflect different levels of memory of the control statistics.

Since the exact distributions of the control statistics are unknown, the *control limits* of the control charts are determined by simulations. The control limit is calibrated to guarantee an $ARL = 100$ in the in-control state, for this purpose we simulate 20000 independent runs of the process to estimate the ARL. The first 20 values of the simulated in-control process are used as burn-in values. The resulting control limits are summarized in Table 1.

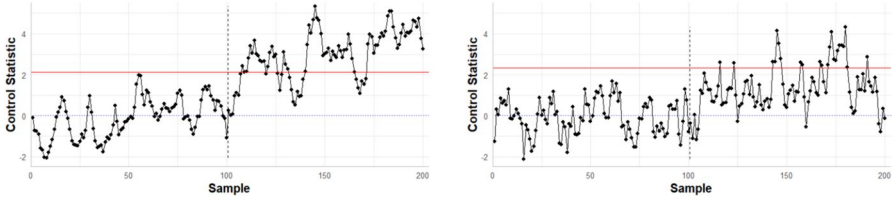


**Fig. 3** Visualization the $CS_1$ chart with $\lambda = 0.2$( left) and $\lambda = 0.5$( right). The shift of the same intensity occurs at sample 101 in both charts

A convenient way to apply a control chart in practice is to plot the control statistics together with the control limit. Figure 3 illustrates the $CS_1$ chart for two values of the smoothing parameter. A later larger (not later) $\lambda$ renders a stronger impact of the most recent sample and a more volatile control statistics.

To check the performance of the control statistics in the out-of-control state, we consider six different scenarios for *possible changes* in different areas of the picture. The mean value of the pixels in a considered area is changed to $f_{i,j} + \delta$ where $\delta \leq 0.05$. Note, that this change is almost impossible to be noticed by the naked eye. The changes were applied to the pixels inside a single ROI, inside neighboring ROIs, inside non-neighboring ROIs, and to the whole picture. The scenarios are:

(a) In this scenario, the changes are applied to the whole picture. Because of the very fast reaction of the control charts, we choose a smaller shift size. Hence,

$$\delta \in \{0.0004, 0.0006, 0.0008, 0.001, 0.002, 0.003, 0.004, 0.005\}.$$

(b) The changes are applied to a square consisting of $60 \times 60$ pixels located at [120 : 180, 120 : 180], which equals $4\%$ of the entire image area. The shift affects nine neighboring ROIs. The performance of the control charts for the described scenario and all the scenarios below (i.e. d– f) is analyzed for $\delta \in \{0.005, 0.01, 0.02, 0.03, 0.04, 0.05\}$.
(c) The changes in the third scenario are applied to $30 \times 30$ pixels located at [11 : 40, 11 : 40], which equals $1\%$ of the entire image area. This change affects four neighboring ROIs.
(d) The changes affect two areas of $15 \times 15$ pixels located at [21 : 35, 21 : 35] and [201 : 215, 201 : 215]. This accounts to $0.5\%$ of the entire image area. The two changed areas are inside separate non-neighboring ROIs.
(e) The changes are applied to $15 \times 15$ pixels located at [21 : 35, 21 : 35]. This covers $0.25\%$ of the entire image and the area is covered by one ROI.
(f) Finally, an area of $15 \times 15$ pixels located at [11 : 25, 11 : 25] is considered, which equals $0.25\%$ of the image. The size of the changed area is the same as in the scenario above, but it affects four neighboring ROIs.

The considered scenarios cover a wide range of possible changes (see Fig. 4). This refers on the one hand to the shape of the areas with shifts and, on the other hand, to the size of the shift. The considered shifted areas differ in size and coverage by

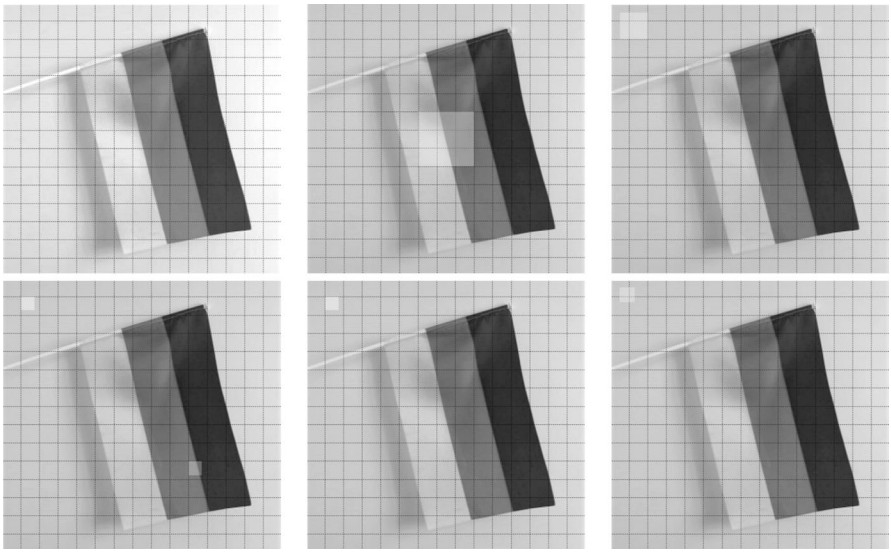

**Fig. 4** Visualization of the different types of changes. 1st row: scenarios (**a**–**c**); 2nd row: scenarios (**d**–**f**)

the ROIs. Since the shape and the size of the ROIs are prespecified in advance, it is important to show the robustness of the charts with respect to their choice. In many cases, the size of the considered shifts is almost invisible to the human eye, but the charts are still capable of detecting it. Note that in all the settings we increase the intensity, i.e. the affected area becomes more white. A reduction of the intensity would be detected with the same speed. However, if the intensity is as well increasing and decreasing within the ROIs, the charts may behave worse since they are based on averaging the values within the ROIs.

The *results* of the simulations were systematically organized into Tables (2, 3, 4, 5, 6, 7), each corresponding to a different change scenario. These tables encapsulate the ARLs of the applied control charts, including differing smoothing parameters. For each specified change, the best (the smallest) ARL values are highlighted in bold. For example, in Table 4 for the change of the intensity $\delta = +0.05$, Control Statistics $CS_{1,t,r}$ with the smoothing parameter $\lambda = 0.2$ performs the best ($ARL = 2.010$)

The simulation study shows that all charts are capable of quickly detecting the shifts in the pixel intensities. There is, however, a subtle difference in the performance that allows us to make *recommendations to practitioners*. First, for small shifts in the intensities, it is appropriate to choose smaller smoothing parameters for any of the charts. This is consistent with the general recommendation for EWMA charts to select smaller values of the parameter $\lambda$ for detecting smaller shifts. The control statistics $CS_{1,t,r}$, $CS_{2,t,r}$, and $CS_{3,t,r}$ have very similar performance, whereas $CS_{3,t,r}$, which is based on the Euclidean distance, seems to react slightly faster [scenarios a), c), e), and f)]. The difference in the performance is still marginal and practitioners can select any of these charts. For all simulated scenarios, the residual control chart $CS^{(r)}_{3,t,r}$ is less successful in detecting shifts in the mean and reacts substantially

**Table 2** ARLs of the control charts based on $CS_{1,t,r}$, $CS_{2,t,r}$, $CS_{3,t,r}$ and $CS^{(r)}_{3,t,r}$

| Change $\delta$ | $\lambda = 0.2$ | | | | $\lambda = 0.5$ | | | |
|---|---|---|---|---|---|---|---|---|
| | $CS_{1,t,r}$ | $CS_{2,t,r}$ | $CS_{3,t,r}$ | $CS^{(r)}_{3,t,r}$ | $CS_{1,t,r}$ | $CS_{2,t,r}$ | $CS_{3,t,r}$ | $CS^{(r)}_{3,t,r}$ |
| +0.0004 | 69.542 | 69.753 | **68.397** | 73.814 | 80.410 | 81.736 | 80.753 | 87.689 |
| +0.0006 | 46.901 | 47.591 | **45.376** | 52.974 | 62.764 | 63.772 | 62.768 | 74.941 |
| +0.0008 | 31.146 | 30.779 | **29.610** | 36.137 | 46.590 | 47.275 | 45.588 | 61.581 |
| +0.001 | 20.479 | 20.506 | **19.809** | 25.083 | 32.648 | 33.384 | 32.024 | 47.034 |
| +0.002 | 5.855 | 5.844 | **5.638** | 7.526 | 6.979 | 7.049 | 6.780 | 11.079 |
| +0.003 | **3.200** | 3.221 | 3.807 | 4.426 | 3.337 | 3.340 | 3.278 | 4.354 |
| +0.004 | **2.183** | 2.199 | 2.315 | 3.258 | 2.243 | 2.260 | 2.229 | 2.704 |
| +0.005 | **1.642** | 1.657 | 1.734 | 2.640 | 1.716 | 1.726 | 1.686 | 2.128 |
| Change $\delta$ | $\lambda = 0.8$ | | | | $\lambda = 1.0$ | | | |
| | $CS_{1,t,r}$ | $CS_{2,t,r}$ | $CS_{3,t,r}$ | $CS^{(r)}_{3,t,r}$ | $CS_{1,t,r}$ | $CS_{2,t,r}$ | $CS_{3,t,r}$ | $CS^{(r)}_{3,t,r}$ |
| +0.0004 | 85.486 | 85.557 | 84.892 | 92.696 | 87.394 | 88.973 | 88.122 | 96.149 |
| +0.0006 | 70.191 | 70.788 | 70.523 | 85.692 | 75.034 | 74.729 | 74.719 | 90.550 |
| +0.0008 | 55.042 | 55.548 | 54.518 | 76.074 | 60.261 | 60.696 | 59.691 | 82.764 |
| +0.001 | 41.458 | 41.093 | 40.303 | 66.472 | 47.447 | 46.841 | 46.117 | 75.262 |
| +0.002 | 8.751 | 8.827 | 8.449 | 23.260 | 10.610 | 10.717 | 10.243 | 34.914 |
| +0.003 | 3.584 | 3.603 | 3.507 | 7.184 | 3.904 | 3.919 | 3.807 | 12.489 |
| +0.004 | 2.279 | 2.286 | 2.236 | 3.018 | 2.358 | 2.356 | 2.315 | 4.321 |
| +0.005 | 1.741 | 1.746 | 1.713 | 1.843 | 1.758 | 1.771 | 1.734 | 1.949 |

The change influences the whole picture (scenario a)

**Table 3** ARLs of the control charts based on $CS_{1,t,r}$, $CS_{2,t,r}$, $CS_{3,t,r}$, and $CS^{(r)}_{3,t,r}$

| Change $\delta$ | $\lambda = 0.2$ | | | | $\lambda = 0.5$ | | | |
|---|---|---|---|---|---|---|---|---|
| | $CS_{1,t,r}$ | $CS_{2,t,r}$ | $CS_{3,t,r}$ | $CS^{(r)}_{3,t,r}$ | $CS_{1,t,r}$ | $CS_{2,t,r}$ | $CS_{3,t,r}$ | $CS^{(r)}_{3,t,r}$ |
| +0.005 | 19.772 | **19.752** | 19.771 | 24.314 | 31.738 | 31.941 | 31.946 | 45.923 |
| +0.01 | 5.678 | 5.651 | **5.638** | 7.342 | 6.696 | 6.750 | 6.642 | 10.771 |
| +0.02 | 2.129 | 2.125 | **2.115** | 3.202 | 2.194 | 2.209 | 2.1928 | 2.650 |
| +0.03 | 1.282 | 1.285 | 1.284 | 2.094 | 1.358 | 1.349 | 1.351 | 1.924 |
| +0.04 | 1.012 | 1.012 | 1.012 | 1.991 | 1.021 | 1.021 | 1.022 | 1.247 |
| +0.05 | 1.0001 | **1.0000** | **1.0000** | 1.499 | **1.0000** | **1.0000** | 1.0001 | 1.0014 |
| Change $\delta$ | $\lambda = 0.8$ | | | | $\lambda = 1.0$ | | | |
| | $CS_{1,t,r}$ | $CS_{2,t,r}$ | $CS_{3,t,r}$ | $CS^{(r)}_{3,t,r}$ | $CS_{1,t,r}$ | $CS_{2,t,r}$ | $CS_{3,t,r}$ | $CS^{(r)}_{3,t,r}$ |
| +0.005 | 40.530 | 40.906 | 40.712 | 65.835 | 45.802 | 46.744 | 45.977 | 74.682 |
| +0.01 | 8.465 | 8.546 | 8.501 | 22.412 | 10.167 | 10.348 | 10.288 | 33.760 |
| +0.02 | 2.241 | 2.229 | 2.233 | 2.904 | 2.292 | 2.296 | 2.288 | 4.128 |
| +0.03 | 1.375 | 1.379 | 1.3682 | **1.279** | 1.387 | 1.380 | 1.381 | 1.185 |
| +0.04 | 1.0224 | 1.0227 | 1.0232 | 1.005 | 1.0252 | 1.0254 | 1.0238 | **1.001** |
| +0.05 | **1.0000** | 1.0001 | 1.0001 | **1.0000** | **1.0000** | 1.0001 | 1.0001 | **1.0000** |

An area of $60 \times 60$ pixels located at [120 : 180, 120 : 180] is influenced by the change (scenario b)

**Table 4** ARLs of the control charts based on $CS_{1,t,r}$, $CS_{2,t,r}$, $CS_{3,t,r}$, and $CS^{(r)}_{3,t,r}$

| Change $\delta$ | $\lambda = 0.2$ | | | | $\lambda = 0.5$ | | | |
|---|---|---|---|---|---|---|---|---|
| | $CS_{1,t,r}$ | $CS_{2,t,r}$ | $CS_{3,t,r}$ | $CS^{(r)}_{3,t,r}$ | $CS_{1,t,r}$ | $CS_{2,t,r}$ | $CS_{3,t,r}$ | $CS^{(r)}_{3,t,r}$ |
| +0.005 | 67.370 | 67.144 | **66.366** | 70.907 | 79.033 | 80.252 | 79.537 | 86.526 |
| +0.01 | 27.961 | 27.733 | **27.728** | 33.161 | 42.872 | 42.932 | 43.150 | 57.243 |
| +0.02 | 7.634 | 7.651 | **7.574** | 9.689 | 10.134 | 10.140 | 10.116 | 17.148 |
| +0.03 | 4.041 | 4.042 | **4.024** | 5.414 | 4.377 | 4.341 | 4.371 | 6.134 |
| +0.04 | **2.697** | 2.715 | 2.700 | 3.863 | 2.803 | 2.801 | 2.794 | 3.473 |
| +0.05 | **2.010** | 2.012 | 2.012 | 3.085 | 2.091 | 2.091 | 2.086 | 2.522 |
| Change $\delta$ | $\lambda = 0.8$ | | | | $\lambda = 1.0$ | | | |
| | $CS_{1,t,r}$ | $CS_{2,t,r}$ | $CS_{3,t,r}$ | $CS^{(r)}_{3,t,r}$ | $CS_{1,t,r}$ | $CS_{2,t,r}$ | $CS_{3,t,r}$ | $CS^{(r)}_{3,t,r}$ |
| +0.005 | 84.211 | 83.754 | 83.599 | 93.202 | 86.065 | 87.434 | 87.108 | 94.572 |
| +0.01 | 52.162 | 52.089 | 51.894 | 74.525 | 57.955 | 58.135 | 57.263 | 81.302 |
| +0.02 | 13.585 | 13.609 | 13.647 | 33.371 | 16.649 | 16.682 | 16.646 | 45.699 |
| +0.03 | 4.992 | 4.979 | 5.002 | 12.203 | 5.720 | 5.758 | 5.689 | 20.202 |
| +0.04 | 2.901 | 2.911 | 2.899 | 4.863 | 3.090 | 3.098 | 3.092 | 8.171 |
| +0.05 | 2.114 | 2.114 | 2.105 | 2.625 | 2.171 | 2.178 | 2.158 | 3.456 |

An area of $30 \times 30$ pixels located at [11 : 40, 11 : 40] is influenced by the change (scenario c)

**Table 5** ARLs of the control charts based on $CS_{1,t,r}$, $CS_{2,t,r}$, $CS_{3,t,r}$, and $CS^{(r)}_{3,t,r}$

| Change $\delta$ | $\lambda = 0.2$ | | | | $\lambda = 0.5$ | | | |
|---|---|---|---|---|---|---|---|---|
| | $CS_{1,t,r}$ | $CS_{2,t,r}$ | $CS_{3,t,r}$ | $CS^{(r)}_{3,t,r}$ | $CS_{1,t,r}$ | $CS_{2,t,r}$ | $CS_{3,t,r}$ | $CS^{(r)}_{3,t,r}$ |
| +0.005 | 84.834 | **82.807** | 84.208 | 85.446 | 91.697 | 91.809 | 90.962 | 93.642 |
| +0.01 | 53.811 | 53.749 | **53.476** | 58.968 | 68.947 | 69.268 | 69.255 | 78.590 |
| +0.02 | **17.612** | 17.663 | 17.793 | 21.532 | 28.528 | 28.583 | 28.490 | 42.427 |
| +0.03 | 8.250 | 8.294 | **8.237** | 10.418 | 11.397 | 11.456 | 11.294 | 19.226 |
| +0.04 | 5.178 | **5.116** | 5.157 | 6.728 | 5.946 | 5.991 | 5.976 | 9.302 |
| +0.05 | 3.698 | 3.704 | **3.679** | 5.033 | 3.916 | 3.929 | 3.949 | 5.321 |
| Change $\delta$ | $\lambda = 0.8$ | | | | $\lambda = 1.0$ | | | |
| | $CS_{1,t,r}$ | $CS_{2,t,r}$ | $CS_{3,t,r}$ | $CS^{(r)}_{3,t,r}$ | $CS_{1,t,r}$ | $CS_{2,t,r}$ | $CS_{3,t,r}$ | $CS^{(r)}_{3,t,r}$ |
| +0.005 | 92.844 | 93.006 | 92.408 | 96.174 | 93.527 | 94.553 | 95.657 | 98.689 |
| +0.01 | 74.099 | 75.686 | 75.140 | 88.162 | 78.838 | 79.205 | 79.592 | 92.895 |
| +0.02 | 36.419 | 36.775 | 36.798 | 61.797 | 42.134 | 42.383 | 42.668 | 71.521 |
| +0.03 | 15.221 | 15.332 | 15.430 | 36.061 | 18.230 | 18.933 | 18.617 | 48.504 |
| +0.04 | 7.260 | 7.256 | 7.351 | 19.040 | 8.715 | 8.681 | 8.702 | 29.681 |
| +0.05 | 4.396 | 4.386 | 4.394 | 10.032 | 4.923 | 4.964 | 4.956 | 16.949 |

Two areas of $15 \times 15$ pixels located at [21 : 35, 21 : 35] and [201 : 215, 201 : 215] are influenced by the change (scenario d)

**Table 6** ARLs of the control charts based on $CS_{1,t,r}$, $CS_{2,t,r}$, $CS_{3,t,r}$, and $CS^{(r)}_{3,t,r}$

| Change $\delta$ | $\lambda = 0.2$ | | | | $\lambda = 0.5$ | | | |
|---|---|---|---|---|---|---|---|---|
| | $CS_{1,t,r}$ | $CS_{2,t,r}$ | $CS_{3,t,r}$ | $CS^{(r)}_{3,t,r}$ | $CS_{1,t,r}$ | $CS_{2,t,r}$ | $CS_{3,t,r}$ | $CS^{(r)}_{3,t,r}$ |
| +0.005 | 92.850 | 92.298 | **91.445** | 92.663 | 94.563 | 96.136 | 94.974 | 97.070 |
| +0.01 | 71.291 | 72.990 | **70.903** | 76.574 | 81.841 | 83.121 | 83.293 | 88.914 |
| +0.02 | 33.3607 | **33.245** | 33.378 | 39.022 | 49.530 | 49.649 | 50.520 | 62.913 |
| +0.03 | **15.670** | 15.693 | 15.734 | 19.396 | 25.072 | 25.354 | 25.471 | 38.388 |
| +0.04 | 9.187 | 9.145 | **9.139** | 11.530 | 13.037 | 13.181 | 13.109 | 22.032 |
| +0.05 | 6.270 | 6.271 | **6.257** | 8.051 | 7.715 | 7.765 | 7.685 | 12.786 |
| Change $\delta$ | $\lambda = 0.8$ | | | | $\lambda = 1.0$ | | | |
| | $CS_{1,t,r}$ | $CS_{2,t,r}$ | $CS_{3,t,r}$ | $CS^{(r)}_{3,t,r}$ | $CS_{1,t,r}$ | $CS_{2,t,r}$ | $CS_{3,t,r}$ | $CS^{(r)}_{3,t,r}$ |
| +0.005 | 96.198 | 96.306 | 96.331 | 98.237 | 96.553 | 97.445 | 97.982 | 98.585 |
| +0.01 | 86.138 | 86.170 | 87.305 | 93.645 | 89.275 | 89.521 | 88.582 | 96.101 |
| +0.02 | 58.135 | 58.281 | 57.833 | 77.824 | 63.594 | 62.888 | 64.097 | 85.842 |
| +0.03 | 33.102 | 32.863 | 33.105 | 58.628 | 38.030 | 38.487 | 38.771 | 68.525 |
| +0.04 | 17.713 | 17.676 | 17.828 | 39.724 | 21.101 | 21.644 | 21.355 | 52.511 |
| +0.05 | 10.054 | 9.952 | 10.005 | 25.923 | 12.051 | 12.277 | 12.137 | 38.317 |

An area of $15 \times 15$ pixels located at [21 : 35, 21 : 35] is influenced by the change (scenario e)

**Table 7** ARLs of the control charts based on $CS_{1,t,r}$, $CS_{2,t,r}$, $CS_{3,t,r}$, and $CS^{(r)}_{3,t,r}$

| Change $\delta$ | $\lambda = 0.2$ | | | | $\lambda = 0.5$ | | | |
|---|---|---|---|---|---|---|---|---|
| | $CS_{1,t,r}$ | $CS_{2,t,r}$ | $CS_{3,t,r}$ | $CS^{(r)}_{3,t,r}$ | $CS_{1,t,r}$ | $CS_{2,t,r}$ | $CS_{3,t,r}$ | $CS^{(r)}_{3,t,r}$ |
| +0.005 | 96.664 | 97.118 | **95.646** | 96.772 | 98.207 | 98.510 | 99.723 | 99.459 |
| +0.01 | 90.304 | **89.455** | 89.553 | 90.557 | 94.532 | 95.551 | 94.314 | 96.500 |
| +0.02 | 66.537 | 67.116 | **66.525** | 70.663 | 79.248 | 80.699 | 79.620 | 86.702 |
| +0.03 | **43.543** | 44.065 | 44.405 | 49.161 | 59.992 | 61.386 | 60.059 | 72.633 |
| +0.04 | 28.127 | **27.463** | 28.024 | 33.373 | 43.364 | 43.783 | 42.744 | 57.426 |
| +0.05 | 18.275 | **18.180** | 18.249 | 22.373 | 29.477 | 29.866 | 29.312 | 43.731 |
| Change $\delta$ | $\lambda = 0.8$ | | | | $\lambda = 1.0$ | | | |
| | $CS_{1,t,r}$ | $CS_{2,t,r}$ | $CS_{3,t,r}$ | $CS^{(r)}_{3,t,r}$ | $CS_{1,t,r}$ | $CS_{2,t,r}$ | $CS_{3,t,r}$ | $CS^{(r)}_{3,t,r}$ |
| +0.005 | 98.784 | 99.448 | 98.781 | 99.203 | 99.346 | 100.338 | 99.662 | 100.163 |
| +0.01 | 95.237 | 94.546 | 95.920 | 98.007 | 97.001 | 97.141 | 96.124 | 96.854 |
| +0.02 | 83.466 | 83.927 | 84.546 | 93.516 | 87.097 | 87.127 | 87.473 | 95.723 |
| +0.03 | 67.404 | 68.850 | 68.593 | 84.467 | 71.994 | 73.451 | 71.931 | 88.776 |
| +0.04 | 51.164 | 52.447 | 51.977 | 73.962 | 57.102 | 57.789 | 57.517 | 80.644 |
| +0.05 | 37.853 | 37.950 | 37.808 | 63.359 | 43.583 | 43.558 | 43.188 | 73.892 |

An area of $15 \times 15$ pixels located at [11 : 25, 11 : 25] is influenced by the change (scenario f)

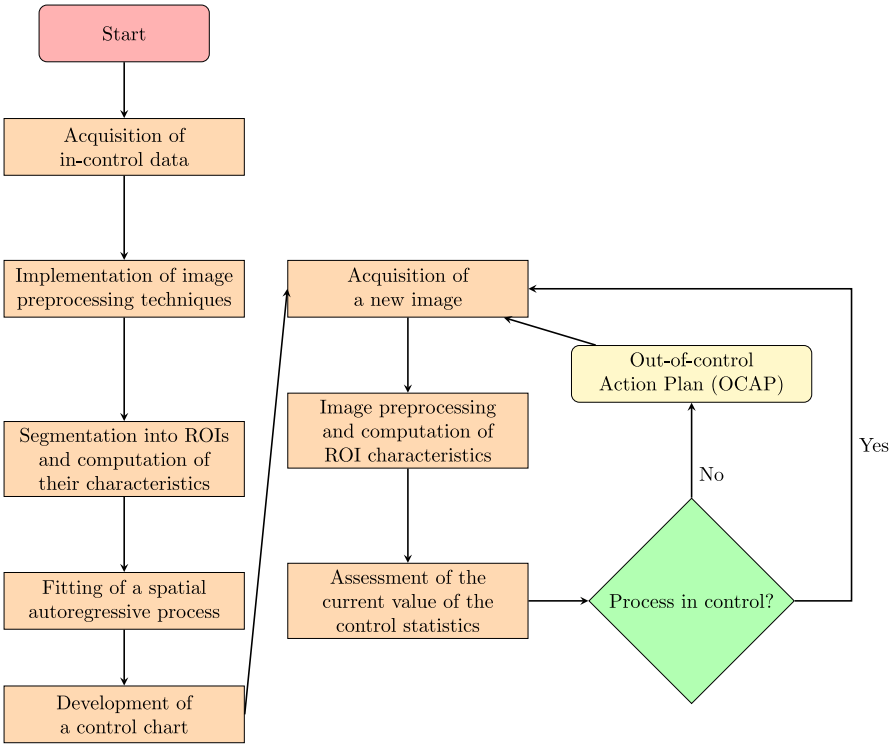


**Fig. 5** Flowchart of the monitoring process with real data

slower in comparison with the other control charts. Since the computational complexity for this chart is much lower, it still can be used for monitoring in settings with time constraints.

## 5 Practical issues

In this section, we summarize the methodological framework, provide recommendations, and discuss practical challenges associated with applying the proposed methodology to real data. The main steps are illustrated in Fig. 5.

In statistical process control, a distinction is made between Phase I and Phase II analysis (cf. Jones-Farmer et al. 2014). Phase I analysis focuses on estimating the unknown process parameters, while Phase II is concerned with monitoring the process using the fitted model from Phase I. The steps involved in Phase I are summarized in the left panel of the flowchart.

We begin by addressing potential issues in Phase I. The initialization of the monitoring process requires in-control data that exhibit no shifts or changes. Although this may seem straightforward, collecting a sufficiently large number of in-control images can be challenging in practice due to the absence of a formal verification process for in-control status or an insufficient sample size. After data collection, it is crucial to

adjust the images to ensure that variations in lighting or camera positioning do not trigger false signals in the control chart. To mitigate such issues, it is recommended to use stationary cameras, permanent lighting, and a fixed object position.

In the next step, the image is decomposed into ROIs. The selection of ROIs is critical for efficient shift detection. Several general approaches can be employed, such as chessboard-type ROIs or expanding squares and rectangles. The optimal choice, however, depends on the nature of the expected changes and the type of image being monitored. Determining the best ROI configuration is left for future research. Finally, a spatial autoregressive process is fitted to the ROI characteristics, followed by the selection of an appropriate control chart. The sample size plays a crucial role in model fitting, as small samples introduce noise into the estimated parameters, potentially leading to false alarms in the control chart due to biased parameter estimates.

Phase II presents fewer challenges compared to Phase I. New images must be preprocessed in a manner consistent with the original in-control data, encompassing both image adjustments and ROI selection. If the analysis of an image suggests that the process is out of control, the out-of-control action plan is initiated. As part of this plan, the practitioner must determine whether the spatial statistical process or the image source requires recalibration. In such cases, a return to Phase I is necessary.

## 6 Conclusions

In this paper, we deal with the problem of detecting shifts in a sequence of images with temporal dependence. We assume that the pixel intensities are subject to an abrupt change, and the aim is to detect this change as soon as possible after its occurrence. This problem arises in industrial quality control if production lines are monitored by cameras. Up to now, it has been assumed that the images are independent in time. It allows to use relatively simple monitoring tools for independent data. In practice, the image data are frequently time-dependent. Another issue that hinders the direct application of established monitoring techniques to image data is the high dimensionality of the problem. High-resolution images are computationally burdensome to handle, so we aggregate the pixels into regions of interest to overcome this challenge. Finally, the pixel intensities exhibit spatial dependence, as neighboring pixels tend to have similar colors. To the best of our knowledge, this is the first paper to propose a statistically rigorous method for monitoring time-dependent, high-resolution image data that exhibits spatial correlation between pixel intensities.

We suggest monitoring the average pixel intensities for the ROIs to reduce the dimensionality and speed up the computations. Furthermore, we develop several EWMA-type control charts that account for temporal dependence and derive explicit analytical results. An extensive simulation study reveals the advantages and weaknesses of the individual charts. Our approach also differs from conventional classification methods used in machine learning, which often ignore spatial correlation and, in many cases, temporal dependence as well. Moreover, our method can detect gradual changes in images and does not require a large number of out-of-control images for training, as is typically necessary for machine learning methods such as convolutional neural networks (CNNs).

The two key issues still require further investigation. First, a data-driven choice of ROI shapes may lead to more efficient shift detection. This refers to both the geometric shape and the size. Second, the spatial covariance matrix estimation is still an unsolved problem in image analysis, and heuristic methods are usually applied. These two open questions are left for future research.

## Appendix

Here we present some theoretical results about the stochastic properties of our control statistics. In Lemma 6.1 and Lemma 6.2 we summarize some results of Bodnar et al. (2023), add some results, and give some minor corrections to the original paper. In Lemma 6.1 the second part of b) and e) is new, and part f) contains a correction of the original paper where an assumption is incorrectly given. In Lemma 6.2 the parts b) to e) are new.

The symbols $\mathrm{a}_{t-\tau}$, $\zeta_{\tau,t,r}$, and $\zeta_{l;\tau,r}$ are used as in (11), i.e.

$$\mathrm{a}_{t-\tau} = (\mathrm{I} - (\mathrm{I} - \boldsymbol{\Lambda})^{t-\tau+1})\mathrm{a} I_{\{0,1,2\ldots\}}(t-\tau), \quad \zeta_{\tau,t,r} = \mathrm{a}'_{t-\tau}\boldsymbol{\Sigma}^{-1}_{t,r}\mathrm{a}_{t-\tau}, \quad \zeta_{l;\tau,r} = \mathrm{a}'\boldsymbol{\Sigma}^{-1}_{l;r}\mathrm{a}\, I_{\mathbb{N}}(\tau). \tag{17}$$

**Proof of Lemma 2.1** Let $\boldsymbol{\Phi} = (\mathrm{I} - \sum_{i=1}^{p} \mathrm{W}_i)^{-1}\mathrm{A}$. Then the Eq. 4 can be written as

$$\boldsymbol{\Gamma}(0) = \boldsymbol{\Phi}\boldsymbol{\Gamma}(0)\boldsymbol{\Phi}' + \left(\mathrm{I} - \sum_{i=1}^{p} \mathrm{W}_i\right)^{-1} \mathrm{G} \left(\mathrm{I} - \sum_{i=1}^{p} \mathrm{W}_i\right)^{-1\prime} \tag{18}$$

and

$$\mathrm{vec}\,(\boldsymbol{\Gamma}(0)) = \mathrm{vec}\,(\boldsymbol{\Phi}\boldsymbol{\Gamma}(0)\boldsymbol{\Phi}') + \mathrm{vec}\left((\mathrm{I} - \sum_{i=1}^{p} \mathrm{W}_i)^{-1}\mathrm{G}\left(\mathrm{I} - \sum_{i=1}^{p} \mathrm{W}_i\right)^{-1\prime}\right).$$

Since $\mathrm{vec}\,(\mathrm{ABC}) = (\mathrm{C}' \otimes \mathrm{A})\,\mathrm{vec}\,(\mathrm{B})$ we get that

$$\mathrm{vec}\,(\boldsymbol{\Gamma}(0)) = (\boldsymbol{\Phi} \otimes \boldsymbol{\Phi})\,\mathrm{vec}\,(\boldsymbol{\Gamma}(0)) + \left(\left(\mathrm{I} - \sum_{i=1}^{p} \mathrm{W}_i\right)^{-1} \otimes \left(\mathrm{I} - \sum_{i=1}^{p} \mathrm{W}_i\right)^{-1}\right) \mathrm{vec}\,(\mathrm{G})$$

with

$$\begin{aligned}\boldsymbol{\Phi}\otimes\boldsymbol{\Phi} &= \left(\left(\mathrm{I}-\sum_{i=1}^{p}\mathrm{W}_i\right)^{-1}\mathrm{A}\right)\otimes\left(\left(\mathrm{I}-\sum_{i=1}^{p}\mathrm{W}_i\right)^{-1}\mathrm{A}\right)\\ &= \left(\left(\mathrm{I}-\sum_{i=1}^{p}\mathrm{W}_i\right)^{-1}\otimes\left(\mathrm{I}-\sum_{i=1}^{p}\mathrm{W}_i\right)^{-1}\right)(\mathrm{A}\otimes\mathrm{A}).\end{aligned}$$

Consequently,

$$\begin{aligned}\mathrm{vec}\ (\boldsymbol{\Gamma}(0)) = &\left(\mathrm{I}-\left(\left(\mathrm{I}-\sum_{i=1}^{p}\mathrm{W}_i\right)^{-1}\otimes\left(\mathrm{I}-\sum_{i=1}^{p}\mathrm{W}_i\right)^{-1}\right)(\mathrm{A}\otimes\mathrm{A})\right)^{-1}\\ &\times\left(\left(\mathrm{I}-\sum_{i=1}^{p}\mathrm{W}_i\right)^{-1}\otimes\left(\mathrm{I}-\sum_{i=1}^{p}\mathrm{W}_i\right)^{-1}\right)\ \mathrm{vec}\ (\mathrm{G}).\end{aligned}$$

Using that $\mathrm{E}^{-1}\otimes\mathrm{E}^{-1}=(\mathrm{E}\otimes\mathrm{E})^{-1}$ and $(\mathrm{I}-\mathrm{C}^{-1}\mathrm{B})^{-1}\mathrm{C}^{-1}=(\mathrm{C}-\mathrm{B})^{-1}$ we obtain

$$\mathrm{vec}\ (\boldsymbol{\Gamma}(0)) = \left(\left(\mathrm{I}-\sum_{i=1}^{p}\mathrm{W}_i\right)\otimes\left(\mathrm{I}-\sum_{i=1}^{p}\mathrm{W}_i\right)-(\mathrm{A}\otimes\mathrm{A})\right)^{-1}\ \mathrm{vec}\ (\mathrm{G}).$$

This completes the proof. □

**Lemma 7.1** *Let* $\{\mathrm{Y}_t\}$ *be a stationary Gaussian process with* $\mathbb{E}(\mathrm{Y}_t)=\boldsymbol{\mu}$ *and* $\mathbb{C}ov(\mathrm{Y}_{t+h},\mathrm{Y}_t)=\boldsymbol{\Gamma}(h)$. *Let* $\tau$ *be fixed.*

(a) Then $T_{1,t,r}\sim\chi^2_{r,\zeta_{\tau,t,r}}$ and

$$\mathbb{E}(T_{1,t,r})=r+\zeta_{\tau,t,r},\mathbb{V}ar(T_{1,t,r})=2(r+2\zeta_{\tau,t,r}).$$

(b) Suppose that $\{\boldsymbol{\Gamma}(v)\}$ is absolutely summable, i.e. that $\sum_{v=0}^{\infty}||\boldsymbol{\Gamma}(v)||<\infty$. Let $r$ be fixed then

$$T_{1,t,r}\xrightarrow[t\to\infty]{d}\chi^2_{r,\zeta_{l;\tau,r}}.$$

If further $\lim_{r\to\infty}\frac{\zeta_{l;\tau,r}}{r}<\infty$, then

$$\lim_{r\to\infty}\lim_{t\to\infty}P\left(\frac{T_{1,t,r}-r-\zeta_{l;\tau,r}}{\sqrt{2(r+2\zeta_{l;\tau,r})}}\le x\right)=N(0,1)(x).$$

(c) Let $t$ be fixed and suppose that $\lim_{r\to\infty}\frac{\zeta_{\tau,t,r}}{r}<\infty$. Then

$$\frac{T_{1,t,r} - r - \zeta_{\tau,t,r}}{\sqrt{2(r + 2\zeta_{\tau,t,r})}} \xrightarrow[r\to\infty]{d} N(0,1).$$

(d) It holds that

$$\begin{aligned}\mathbb{E}(T_{2,t,r}) =& \mathrm{tr}(\boldsymbol{\Sigma}_{l;r}^{-1}\boldsymbol{\Sigma}_{t,r}) + \mathrm{a}'_{t-\tau}\boldsymbol{\Sigma}_{l;r}^{-1}\mathrm{a}_{t-\tau},\\ \mathbb{V}ar(T_{2,t,r}) =& 2\mathrm{tr}((\boldsymbol{\Sigma}_{l;r}^{-1}\boldsymbol{\Sigma}_{t,r})^2) + 4\mathrm{a}'_{t-\tau}\boldsymbol{\Sigma}_{l;r}^{-1}\boldsymbol{\Sigma}_{t,r}\boldsymbol{\Sigma}_{l;r}^{-1}\mathrm{a}_{t-\tau}.\end{aligned}$$

(e) Suppose that $\{\boldsymbol{\Gamma}(v)\}$ is absolutely summable. Let $r$ be fixed and let

$$\lim_{t\to\infty} \boldsymbol{\Sigma}_{t,r}^{1/2} = \boldsymbol{\Sigma}_{l;r}^{1/2} \tag{19}$$

then

$$T_{2,t,r} \xrightarrow[t\to\infty]{d} \chi^2_{r,\zeta_{l;\tau,r}}.$$

If further $\lim_{r\to\infty} \frac{\zeta_{l;\tau,r}}{r} < \infty$, then

$$\lim_{r\to\infty}\lim_{t\to\infty} P\left(\frac{T_{2,t,r} - r - \zeta_{l;\tau,r}}{\sqrt{2(r + 2\zeta_{l;\tau,r})}} \le x\right) = N(0,1)(x).$$

(f) Let $t$ be fixed. Suppose that $\mathrm{U}_{l;t,r}$ is an orthogonal matrix such that

$$\mathrm{U}'_{l;t,r}\boldsymbol{\Sigma}_{t,r}^{1/2}\boldsymbol{\Sigma}_{l;r}^{-1}\boldsymbol{\Sigma}_{t,r}^{1/2}\mathrm{U}_{l;t,r} = \ \mathrm{diag}\ (\lambda_{l;t,r,1},\ldots,\lambda_{l;t,r,r})$$

and let $\mathrm{U}'_{l;t,r}\boldsymbol{\Sigma}_{t,r}^{-1/2}\mathrm{a}_{t-\tau} = (\delta_{l;t,r,1},\ldots,\delta_{l;t,r,r})'$. If

$$\lim_{r\to\infty} \frac{\max_{1\le i\le r}\lambda^2_{l;t,r,i}(1 + 2\delta^2_{l;t,r,i})}{\sum_{i=1}^{p}\lambda^2_{l;t,r,i}(1 + 2\delta^2_{l;t,r,i})} = 0 \tag{20}$$

then

$$\frac{T_{2,t,r} - \mathrm{tr}(\boldsymbol{\Sigma}_{l;r}^{-1}\boldsymbol{\Sigma}_{t,r}) - \mathrm{a}'_{t-\tau}\boldsymbol{\Sigma}_{l;r}^{-1}\mathrm{a}_{t-\tau}}{\sqrt{2(\mathrm{tr}((\boldsymbol{\Sigma}_{l;r}^{-1}\boldsymbol{\Sigma}_{t,r})^2) + 4\mathrm{a}'_{t-\tau}\boldsymbol{\Sigma}_{l;r}^{-1}\boldsymbol{\Sigma}_{t,r}\boldsymbol{\Sigma}_{l;r}^{-1}\mathrm{a}_{t-\tau}}} \xrightarrow[r\to\infty]{d} N(0,1).$$

***Proof*** The second part of b) follows directly with Lemma 4 of Bodnar and Reiss (2016).

In order to prove e) we use that $\mathrm{Z}_t - \boldsymbol{\mu} \sim \mathcal{N}_r(\mathrm{a}_{t-\tau}, \boldsymbol{\Sigma}_{t,r})$ and that

$$(\mathrm{Z}_t-\boldsymbol{\mu})'\boldsymbol{\Sigma}_{l;r}^{-1}(\mathrm{Z}_t-\boldsymbol{\mu})=\left(\boldsymbol{\Sigma}_{t,r}^{-1/2}(\mathrm{Z}_t-\boldsymbol{\mu})\right)'\boldsymbol{\Sigma}_{t,r}^{1/2}\boldsymbol{\Sigma}_{l;r}^{-1}\boldsymbol{\Sigma}_{t,r}^{1/2}\left(\boldsymbol{\Sigma}_{t,r}^{-1/2}(\mathrm{Z}_t-\boldsymbol{\mu})\right)$$

We observe that $\boldsymbol{\Sigma}_{t,r}^{-1/2}(\mathrm{Z}_t-\boldsymbol{\mu})\sim\mathcal{N}_r(\boldsymbol{\Sigma}_{t,r}^{-1/2}\mathrm{a}_{t-\tau},\mathrm{I})$. Because of (19) we get that $\boldsymbol{\Sigma}_{t,r}^{1/2}\boldsymbol{\Sigma}_{l;r}^{-1}\boldsymbol{\Sigma}_{t,r}^{1/2}\xrightarrow{t\to\infty}\mathrm{I}$ and the first part of a) is proved.

In order to prove f) we use that $\mathrm{Z}_t-\boldsymbol{\mu}\sim\mathcal{N}_r(\mathrm{a}_{t-\tau},\boldsymbol{\Sigma}_{t,r})$ and that

$$\begin{aligned}(\mathrm{Z}_t-\boldsymbol{\mu})'\boldsymbol{\Sigma}_{l;r}^{-1}(\mathrm{Z}_t-\boldsymbol{\mu})&=\left(\boldsymbol{\Sigma}_{t,r}^{-1/2}(\mathrm{Z}_t-\boldsymbol{\mu})\right)'\boldsymbol{\Sigma}_{t,r}^{1/2}\boldsymbol{\Sigma}_{l;r}^{-1}\boldsymbol{\Sigma}_{t,r}^{1/2}\left(\boldsymbol{\Sigma}_{t,r}^{-1/2}(\mathrm{Z}_t-\boldsymbol{\mu})\right)\\&=\left(\mathrm{U}_{l;t,r}'\boldsymbol{\Sigma}_{t,r}^{-1/2}(\mathrm{Z}_t-\boldsymbol{\mu})\right)'\mathrm{U}_{l;t,r}'\boldsymbol{\Sigma}_{t,r}^{1/2}\boldsymbol{\Sigma}_{l;r}^{-1}\boldsymbol{\Sigma}_{t,r}^{1/2}\mathrm{U}_{l;t,r}\left(\mathrm{U}_{l;t,r}\boldsymbol{\Sigma}_{t,r}^{-1/2}(\mathrm{Z}_t-\boldsymbol{\mu})\right)\\&=\sum_{i=1}^{r}\lambda_{l;t,r,i}H_{l;t,r,i}^2\end{aligned}$$

with $(H_{l;t,r,i})_{i=1,..,r}\sim\mathcal{N}_r((\delta_{l;t,r,i})_{i=1,..,r},\mathrm{I})$. Following the proof of Lemma 2 of Bodnar et al. (2023) we make use of Lemma 4 of Bodnar et al. (2023). To apply this Lemma we need that (20) holds. □

Note that the condition (19) is fulfilled if, e.g., all eigenvalues of $\boldsymbol{\Sigma}_{l;r}$ are simple. If, e.g.,

$$\mathrm{U}_{Eu;t,r}'\boldsymbol{\Sigma}_{t,r}\mathrm{U}_{Eu;t,r}=\ \mathrm{diag}\ (\lambda_{Eu;t,r,1},\ldots,\lambda_{Eu;t,r,r})$$

then

$$\boldsymbol{\Sigma}_{t,r}^{1/2}=\mathrm{U}_{Eu;t,r}\ \mathrm{diag}\ (\sqrt{\lambda_{Eu;t,r,1}},\ldots,\sqrt{\lambda_{Eu;t,r,r}})\mathrm{U}_{Eu;t,r}'.$$

$\mathrm{U}_{Eu;t,r}$ consists of the normalized eigenvectors which could be chosen to be continuous in the case of simple eigenvalues if $t$ is sufficiently large. This is in principle a result of the implicit function theorem. Thus the matrix converges to $\boldsymbol{\Sigma}_{l;r}^{1/2}$. We refer to Lax (2007) for more discussions.

**Lemma 7.2** *Let* $\{\mathrm{Y}_t\}$ *be a stationary Gaussian process with* $\mathbb{E}(\mathrm{Y}_t)=\boldsymbol{\mu}$ *and* $\mathbb{C}ov(\mathrm{Y}_{t+h},\mathrm{Y}_t)=\boldsymbol{\Gamma}(h)$. *Let* $\tau$ *be fixed.*

(a) If $r$ is fixed then

$$\begin{aligned}\mathbb{E}((\mathrm{Z}_t-\boldsymbol{\mu})'(\mathrm{Z}_t-\boldsymbol{\mu}))&=\mathrm{tr}(\boldsymbol{\Sigma}_{t,r})+\mathrm{a}_{t-\tau}'\mathrm{a}_{t-\tau}\\&\xrightarrow[t\to\infty]{}\quad\mathrm{tr}(\boldsymbol{\Sigma}_{l;r})+\mathrm{a}'\mathrm{a}I_{\mathbb{N}}(\tau),\\\mathbb{V}ar((\mathrm{Z}_t-\boldsymbol{\mu})'(\mathrm{Z}_t-\boldsymbol{\mu}))&=2\mathrm{tr}(\boldsymbol{\Sigma}_{t,r}^2)+4\mathrm{a}_{t-\tau}'\boldsymbol{\Sigma}_{t,r}\mathrm{a}_{t-\tau}\\&\xrightarrow[t\to\infty]{}\quad2\mathrm{tr}(\boldsymbol{\Sigma}_{l;r}^2)+4\mathrm{a}'\boldsymbol{\Sigma}_{l;r}\mathrm{a}I_{\mathbb{N}}(\tau).\end{aligned}$$

(b) Let $r$ be fixed and let $\mathrm{U}_{EU;t,r}$ be an orthogonal matrix such that

$$\mathrm{U}'_{Eu;t,r}\boldsymbol{\Sigma}_{t,r}\mathrm{U}_{Eu;t,r} = \ \mathrm{diag}\ (\lambda_{Eu;t,r,1},\ldots,\lambda_{Eu;t,r,r})$$

then

$$(\mathrm{Z}_t-\boldsymbol{\mu})'(\mathrm{Z}_t-\boldsymbol{\mu})\overset{d}{=}\sum_{i=1}^{r}\lambda_{Eu;t,r,i}H^2_{Eu;t,r,i}$$

with $(H_{Eu;t,r,i})_{i=1,\ldots,r}\sim\mathcal{N}_r(\mathrm{U}'_{Eu;t,r}\boldsymbol{\Sigma}^{-1/2}_{t,r}\mathrm{a}_{t-\tau},\mathrm{I})$.

(c) Suppose that $\{\boldsymbol{\Gamma}(v)\}$ is absolutely summable. Let $r$ be fixed and $\mathrm{U}_{Eu;l,r}$ be an orthogonal matrix such that

$$\mathrm{U}'_{Eu;l,r}\boldsymbol{\Sigma}_{l;r}\mathrm{U}_{Eu;l,r} = \ \mathrm{diag}\ (\lambda_{Eu;l,r,1},\ldots,\lambda_{Eu;l,r,r}).$$

If

$$\lim_{t\to\infty}\mathrm{U}_{Eu;t,r}=\mathrm{U}_{Eu;l,r} \tag{21}$$

then

$$(\mathrm{Z}_t-\boldsymbol{\mu})'(\mathrm{Z}_t-\boldsymbol{\mu})\ \xrightarrow[t\to\infty]{d}\ \sum_{i=1}^{r}\lambda_{Eu;l,r,i}H^2_{Eu;l,r,i}$$

with $(H_{Eu;l,r,i})_{i=1,\ldots,r}\sim\mathcal{N}_r(\boldsymbol{\delta}_{Eu;l,r},\mathrm{I})$, $\boldsymbol{\delta}_{Eu;l,r}=(\delta_{Eu;l,r,i})_{i=1,\ldots,r}=\mathrm{U}'_{Eu;l,r}\boldsymbol{\Sigma}^{-1/2}_{l;r}\mathrm{a}I_{\mathbb{N}}(\tau)$. If further

$$\lim_{r\to\infty}\frac{\max_{1\le i\le r}\lambda^2_{Eu;l,r,i}(1+2\delta^2_{Eu;l,r,i})}{\sum_{i=1}^{r}\lambda^2_{Eu;l,r,i}(1+2\delta^2_{Eu;l,r,i})}=0$$

then

$$\lim_{r\to\infty}\lim_{t\to\infty}P\Big(\frac{(\mathrm{Z}_t-\boldsymbol{\mu})'(\mathrm{Z}_t-\boldsymbol{\mu})-\mathrm{tr}(\boldsymbol{\Sigma}_{l;r})-\mathrm{a}'\mathrm{a}I_{\mathbb{N}}(\tau)}{\sqrt{2\mathrm{tr}(\boldsymbol{\Sigma}^2_{l;r})+4\mathrm{a}'\boldsymbol{\Sigma}_{l;r}\mathrm{a}I_{\mathbb{N}}(\tau)}}\le x\Big)=N(0,1)(x).$$

(d) Let $t$ be fixed. Suppose that

$$\frac{\max_{1\le i\le r}\lambda^2_{Eu;t,r,i}(1+2\delta^2_{Eu;t,r,i})}{\sum_{v=1}^{r}\lambda^2_{Eu;t,r,v}(1+2\delta^2_{Eu;t,r,v})}\ \xrightarrow[r\to\infty]{}\ 0 \tag{22}$$

then

$$\frac{(\mathrm{Z}_t-\boldsymbol{\mu})'(\mathrm{Z}_t-\boldsymbol{\mu})-\mathrm{tr}\,(\boldsymbol{\Sigma}_{t,r})-\mathrm{a}'_{t-\tau}\mathrm{a}_{t-\tau}}{\sqrt{2\mathrm{tr}(\boldsymbol{\Sigma}^2_{t,r})+4\mathrm{a}'_{t-\tau}\boldsymbol{\Sigma}_{t,r}\mathrm{a}_{t-\tau}}}\ \xrightarrow[r\to\infty]{d}\ N(0,1). \tag{23}$$

***Proof*** To prove part b) we use that

$$(\mathrm{Z}_t - \boldsymbol{\mu})'(\mathrm{Z}_t - \boldsymbol{\mu}) = \left(\mathrm{U}'_{Eu;t,r}\boldsymbol{\Sigma}_{t,r}^{-1/2}(\mathrm{Z}_t - \boldsymbol{\mu})\right)' \mathrm{U}'_{Eu;t,r}\boldsymbol{\Sigma}_{t,r}\mathrm{U}_{Eu;t,r}$$
$$\left(\mathrm{U}'_{Eu;t,r}\boldsymbol{\Sigma}_{t,r}^{-1/2}(\mathrm{Z}_t - \boldsymbol{\mu})\right) = \sum_{i=1}^{r} \lambda_{Eu;t,r,i} H^2_{Eu;t,r,i}.$$

To prove part c) we use that the eigenvalues of a matrix are continuous functions of the elements of the matrix (cf. Lax 2007). Using (21) we get that

$$\boldsymbol{\Sigma}_{t,r}^{1/2} = \mathrm{U}'_{Eu;t,r}\ \mathrm{diag}\ (\sqrt{\lambda_{Eu;t,r,1}}, \ldots, \sqrt{\lambda_{Eu;t,r,r}})\mathrm{U}_{Eu;t,r}$$
$$\xrightarrow[t\to\infty]{} \mathrm{U}'_{Eu;l,r}\ \mathrm{diag}\ (\sqrt{\lambda_{Eu;l,r,1}}, \ldots, \sqrt{\lambda_{Eu;l,r,r}})\mathrm{U}_{Eu;l,r} = \boldsymbol{\Sigma}_{l;r}^{1/2}$$

and the result follows.

The second part of c) follows again with Bodnar and Reiss (2016).

Part d) is proved in Bodnar et al. (2023) but here the condition (22) is correctly formulated. □

In the proofs of Lemma 6.1 and Lemma 6.2 we make use of the fact that the eigenvalues of a matrix are continuous functions of the elements of a matrix (cf. Theorem 9.6 of Lax 2007). Note that the eigenvectors of a matrix may not be continuous functions of the elements of the underlying matrix. This point is analyzed in detail in, e.g., chapter 9 of Lax (2007). A sufficient condition for (21) to hold is that all eigenvalues of $\boldsymbol{\Sigma}_{l;r}$ are simple.

**Funding** Open Access funding enabled and organized by Projekt DEAL. Open Access funding enabled and organized by Projekt DEAL. Open Access funding enabled and organized by Projekt DEAL. The authors acknowledge the financial support of the Deutsche Forschungsgemeinschaft (DFG, German Research Foundation) project number 428472210.

## Declarations

**Conflict of interest** The authors declare that they have no conflict of interest.

## References


Alwan LC, Roberts HV (1988) Time-series modeling for statistical process control. J Bus Econ Stat 6(1):87–95 (**ISSN 07350015**)

Alwan LC, Roberts HV (1995) The problem of misplaced control limits. J Roy Stat Soc Ser C (Appl Stat) 44(3):269–278

Amirkhani F, Amiri A (2020) A novel framework for spatiotemporal monitoring and post-signal diagnosis of processes with image data. Qual Reliab Eng Int 36(2):705–735

Anselin L (2010) Thirty years of spatial econometrics. Pap Reg Sci 89(1):3–25

Armingol JM, Otamendi J, De La Escalera A, Pastor JM, Rodriguez FJ (2003) Statistical pattern modeling in vision-based quality control systems. J Intell Rob Syst 37(3):321–336

Bai Z, Saranadasa H (1996) Effect of high dimension: by an example of a two sample problem. Stat Sin 6(2):311–329

Bodnar T, Reiss M (2016) Exact and asymptotic tests on a factor model in low and large dimensions with applications. J Multivar Anal 150:125–151

Bodnar R, Bodnar T, Schmid W (2023) Sequential monitoring of high-dimensional time series. Scand J Stat 50:962–992

Bodnar R, Bodnar T, Schmid W (2024) Control charts for high-dimensional time series with estimated in-control parameters. Forthcom Seq Anal 43(1):103–129

Brockwell PJ, Davis RA (1991) Time series: theory and methods. Springer, New York

Chen SX, Qin Y-L (2010) A two-sample test for high-dimensional data with applications to gene-set testing. Ann Stat 38(2):808–835

Chen S, Wells L (2022) A multi-image monitoring framework for statistical process control to improve manufacturing systems. Qual Reliab Eng Int 38(2):679–702

Chen R, Xiao H, Yang D (2021) Autoregressive models for matrix-valued time series. J Econom 222(1):539–560

Cressie N, Wikle CK (2011) Statistics for Spatio-temporal data. Wiley, Hoboken

Dastoorian R, Wells LJ (2023) A hybrid off-line/on-line quality control approach for real-time monitoring of high-density datasets. J Intell Manuf 34(2):669–682

Dastoorian R, Wells L, Shafae M (2022) Assessing the performance of control charts for detecting previously unexplored shift types in high density spatial data. Qual Eng 34(1):125–141

Does R, Goedhart R, Woodall W (2022) On the design of control charts with guaranteed conditional performance under estimated parameters. Qual Reliab Eng Int 36:2610–2620

Ekström S-E, Serra-Capizzano S (2018) Eigenvalues and eigenvectors of banded Toeplitz matrices and the related symbols. Num Linear Algebra Appl 25(5):e2137

Elhorst JP (2010) Applied spatial econometrics: raising the bar. Spat Econ Anal 5(1):9–28

Eslami D, Izadbakhsh H, Ahmadi O, Zarinbal M (2023) Spatial-nonparametric regression: an approach for monitoring image data. Commun Stat Theory Methods 52(12):4114–4137

Fieguth P (2010) Statistical image processing and multidimensional modeling. Springer, New York

Garza-Venegas JA, Tercero-Gómez VG, Ho LL, Castagliola P, Celano G (2018) Effect of autocorrelation estimators on the performance of the [CDATA[{\bar{x}}]]$\bar{x}$ control chart. J Stat Comput Simul 88(13):2612–2630

Hallin M, Lippi M, Barigozzi M, Forni M, Zaffaroni P (2020) Time series in high dimensions: the general dynamic factor model. World Scientific, Singapore

Horst R, Negin M (1992) Vision system for high-resolution dimensional measurements and on-line SPC: web process application. IEEE Trans Ind Appl 28(4):993–997

Jensen WA, Jones-Farmer LA, Champ CW, Woodall WH (2006) Effects of parameter estimation on control chart properties: a literature review. J Qual Technol 38(4):349–364

Jiang B, Wang C, Liu H (2005) Liquid crystal display surface uniformity defect inspection using analysis of variance and exponentially weighted moving average techniques. Int J Prod Res 43(1):67–80

Jones-Farmer LA, Jordan VB, Woodall WH (2014) An overview of phase i analysis for process improvement and monitoring. J Qual Technol 46(3):265–280

Kitagawa G (1977) An algorithm for solving the matrix equation $X = FXF^T + S$[CDATA[X = FXF^T +S]]. Int J Control 25(5):745–753

Knoth S, Schmid W (2004) Control charts for time series: a review. In Frontiers in Statistical Quality Control, vol. 7Springer, New York, pp 210–236. (**ISBN 978-3-7908-2674-6**)

Koosha M, Noorossana R, Megahed F (2017) Statistical process monitoring via image data using wavelets. Qual Reliab Eng Int 33(8):2059–2073
Kramer HG, Schmid W (1997) EWMA charts for multivariate time series. Seq Anal 16(2):131–154
Kramer H, Schmid W (2000) The influence of parameter estimation on the arl of shewhart-type charts for time series, statistical papers. Stat Pap 41:173–196
Lax PD (2007) Linear algebra and its applications. Wiley, Hoboken
LeSage J, Pace RK (2009) Introduction to spatial econometrics. Chapman and Hall/CRC, Boca Raton
Lin H-D (2007) Automated visual inspection of ripple defects using wavelet characteristic based multivariate statistical approach. Image Vis Comput 25(11):1785–1801
Lin H-D (2007) Computer-aided visual inspection of surface defects in ceramic capacitor chips. J Mater Process Technol 189(1–3):19–25
Lin H-D, Chung C-Y, Lin W-T (2008) Principal component analysis based on wavelet characteristics applied to automated surface defect inspection. WSEAS Trans Comput Res 3(4):193–202
Liu JJ, MacGregor JF (2006) Estimation and monitoring of product aesthetics: application to manufacturing of "engineered stone" countertops. Mach Vis Appl 16(6):374
Lowry CA, Woodall WH, Champ CW, Rigdon SE (1992) A multivariate exponentially weighted moving average control chart. Technometrics 34(1):46–53
Lu C-J, Tsai D-M (2005) Automatic defect inspection for LCDs using singular value decomposition. Int J Adv Manuf Technol 25(1–2):53–61
Mason RL, Tracy ND, Young JC (1997) A practical approach for interpreting multivariate $T^2$ [CDATA[{T}^2]] control chart signals. J Qual Technol 29(4):396–406
Megahed FM, Woodall WH, Camelio JA (2011) A review and perspective on control charting with image data. J Qual Technol 43(2):83–98
Megahed FM, Wells LJ, Camelio JA, Woodall WH (2012) A spatiotemporal method for the monitoring of image data. Qual Reliab Eng Int 28(8):967–980
Okhrin Y, Schmid W (2007) Comparison of different estimation techniques for portfolio selection. AStA Adv Stat Anal 91(2):109–127
Okhrin Y, Schmid W, Semeniuk I (2020) New approaches for monitoring image data. IEEE Trans Image Process 30:921–933
Okhrin Y, Schmid W, Semeniuk I (2021) Monitoring image processes: overview and comparison study. In: Knoth S, Schmid W (eds) Frontiers in statistical quality control, vol 13. Springer, New York, pp 143–163
Okhrin Y, Petruk V, Schmid W (2025) Spatial averaging of var processes for image analysis. Submitted for publication
Psarakis S, Vyniou AK, Castagliola P (2014) Some recent developments on the effects of parameter estimation on control charts. Qual Reliab Eng Int 30(8):1113–1129
Roy A, Mukherjee PS (2025) Upper quantile-based cusum-type control chart for detecting small changes in image data. J Appl Stat, 0(0):1–16
Schmid W (1995) On the run length of a Shewhart chart for correlated data. Stat Pap 36(1):111–130
Schmid W (1997) On EWMA charts for time series. In: Lenz H-J, Wilrich P-T (eds) Frontiers in statistical quality control, vol 5. Springer, New York, pp 115–137
Tong L-I, Wang C-H, Huang C-L (2005) Monitoring defects in IC fabrication using a Hotelling $T^2$ [CDATA[{T}^2]] control chart. IEEE Trans Semicond Manuf 18(1):140–147
Wang D, Liu X, Chen R (2019) Factor models for matrix-valued high-dimensional time series. J Econom 208(1):231–248
Yao J, Balasubramaniam B, Li B, Kreiger EL, Wang C (2024) Adaptive sampling and monitoring of partially observed images. J Qual Technol 56(2):157–173
Yeganeh A, Shadman A (2021) Using evolutionary artificial neural networks in monitoring binary and polytomous logistic profiles. J Manuf Syst 61:546–561 (**ISSN 0278-6125**)
Yeganeh A, Johannssen A, Chukhrova N (2024) The partitioning ensemble control chart for on-line monitoring of high-dimensional image-based quality characteristics. Eng Appl Artif Intell 127:107282